13. Hata H, Matsumiya G, Miyagawa S, et al. Grafted skeletal myoblast sheets attenuate myocardial remodeling in pacing-induced canine heart failure model. *J Thoracic Cardiovasc Surg* 2006; 132: 918.
14. Sekiya N, Matsumiya G, Miyagawa S, et al. Layered implantation of myoblast sheets attenuates adverse cardiac remodeling of the infracted heart. *J Thorac Cardiovasc Surg* 2009; 138: 985.
15. Kitagawa-Sakakida S, Tori M, Li Z, et al. Active cell migration in retransplanted rat cardiac allografts during the course of chronic rejection. *J Heart Lung Transplant* 2000; 19: 584.
16. Nishina T, Nishimura K, Yuasa S, et al. Initial effects of the left ventricular repair by placation may not last long in a rat ischemic cardiomyopathy model. *Circulation* 2001; 104: I-241.
17. Miyagawa S, Sawa Y, Taketani S, et al. Myocardial regeneration therapy for heart failure. Hepatocyte growth factor enhances the effect of cellular cardiomyoplasty. *Circulation* 2002; 105: 2556.
18. Shudo Y, Miyagawa S, Fukushima S, et al. Novel regenerative therapy using cell-sheet covered with omentum flap delivers a huge number of cells in a porcine myocardial infarction model. *J Thorac Cardiovasc Surg* 2011; 142: 1199.
19. Askari AT, Unzek S, Penn MMS, et al. Effect of stromal-cell-derived factor 1 on stem-cell homing and tissue regeneration in ischemic cardiomyopathy. *Lancet* 2003; 362: 97.
20. Miyagawa S, Roth M, Saito A, et al. Tissue-engineered cardiac constructs for cardiac repair. *Ann Thorac Surg* 2011; 91: 320.
21. Ratajczak MZ, Peier S, Janowska WA, et al. Expression of functional CXCR4 by muscle satellite cells and secretion of SDF-1 by muscle-derived fibroblasts is associated with the presence of both muscle progenitors in bone marrow and hematopoietic stem/progenitor cells in muscles. *Stem Cells* 2003; 21: 363.
22. Taniyama Y, Morishita R, Aoki M, et al. Angiogenesis and antifibrotic action by hepatocyte growth factor in cardiomyopathy. *Hypertension* 2002; 40: 47.
23. Shimizu T, Okamoto H, Chiba S, et al. VEGF-mediated angiogenesis is impaired by angiotensin type 1 receptor blockade in cardiomyopathic hamster hearts. *Cardiovasc Res* 2003; 58: 203.
24. Hoashi T, Matsumiya G, Miyagawa S, et al. Skeletal myoblast sheet transplantation improves the diastolic function of a pressure-overloaded right heart. *J Thorac Cardiovasc Surg* 2009; 138: 460.
25. Nakajima H, Nakajima HO, Salcher O, et al. Atrial but not ventricular fibrosis in mice expressing a mutant transforming growth factor-beta(1) transgene in the heart. *Circ Res* 2000; 86: 571.
26. Pokharel S, Rasoul S, Roks AJ, et al. *N*-acelyl-Ser-Asp-Lys-Pro inhibits phosphorylation of Smad2 in cardiac fibrosis. *Hypertension* 2002; 40: 155.
27. Oh J, Takahashi R, Kondo S, et al. The membrane-anchored MMP inhibitor RECK is a key regulator of extracellular matrix integrity and angiogenesis. *Cell* 2001; 107: 789.
28. Nomoto T, Nishina T, Miwa S, et al. Angiotensin-converting enzyme inhibitor helps prevent late remodeling after left ventricular aneurysm repair in rats. *Circulation* 2002; 106: I-115.
29. Kanemitsu H, Takai S, Tsuneyoshi H, et al. Chronic chymase inhibition preserves cardiac function after left ventricular repair in rats. *Eur J Cardiothorac Surg* 2008; 33: 25.
30. Sakakibara Y, Tambara K, Lu F, et al. Combined procedure of surgical repair and cell transplantation for left ventricular aneurysm: An experimental study. *Circulation* 2002; 106: I-193.
31. Sato T, Shishido T, Kawada T, et al. ESPVR of in situ rat left ventricle shows contractility-dependent curvilinearity. *Am J Physiol* 1998; 274: 1429.

Journal of Bioscience and Bioengineering
VOL. 113 No. 1, 128–131, 2012

ELSEVIER

www.elsevier.com/locate/jbiosc

TECHNICAL NOTE

Evaluation of vertical cell fluidity in a multilayered sheet of skeletal myoblasts

Masahiro Kino-oka,[1,*] Trung Xuan Ngo,[2] Eiji Nagamori,[1] Yasunori Takezawa,[2] Yasuki Miyake,[2] Yoshiki Sawa,[3] Atsuhiro Saito,[3] Tatsuya Shimizu,[4] Teruo Okano,[4] and Masahito Taya[2]

Department of Biotechnology, Graduate School of Engineering, Osaka University, 2-1 Yamada-oka, Suita, Osaka 565-0871, Japan,[1] Division of Chemical Engineering, Graduate School of Engineering Science, Osaka University, 1-3 Machikaneyama-cho, Toyonaka, Osaka 560-8531, Japan,[2] Department of Surgery, Division of Cardiovascular Surgery, Graduate School of Medicine, Osaka University, 2-15 Yamada-oka, Suita, Osaka 565-0871, Japan,[3] and Institute of Advanced Biomedical Engineering and Science, Tokyo Women's Medical University, 8-1 Kawada-cho, Shinjuku-ku, Tokyo 162-8666, Japan[4]

Received 19 August 2011; accepted 5 September 2011
Available online 20 October 2011

The procedure for fabricating a multilayered cell sheet has been developed by combining multiple sheets using a thermo-responsive surface and stamp system. Confocal laser scanning microscopy revealed that the fluidity of a multilayered sheet of skeletal myoblasts could be estimated as vertical diffusivity and changed upon addition of dermal fibroblasts.

[**Key words:** Cell sheet; Skeletal myoblasts; Dermal fibroblasts; Cell migration; Sheet fluidity; Image processing]

Cell sheet engineering is emerging as an advanced technique for preparing scaffold-free 3-dimensional (3-D) tissue (1), not only for transplantation but also for *in vitro* research. A temperature-responsive poly-*N*-isopropylacrylamide (PIPAAm) grafted surface can be used to form a cell sheet without any enzymatic digestion, thereby which permits to retain an intact extracellular matrix (ECM) (1). Sasagawa et al. previously constructed a multilayered structure of skeletal muscle myoblast cells in which prevascular formation by endothelial migration was observed (2).

Cell migration in 3-D constructs plays an important role in physiological and pathological phenomena such as embryonic development, cell alignment, immune reaction, angiogenesis, and metastasis (3). Understanding the mechanisms of cell migration will be useful in the design of biomimetic structures and functional engineered tissues. Although the behaviors of cells on 2-D culture surfaces have been extensively investigated (4–7), spatial cell movement in 3-D tissues, especially with regard to vertical migration inside the tissue, has not been investigated due to the absence of methods to allow *in vitro* quantitative and reproducible measurements. In the present study, a five-layered skeletal myoblast sheet was fabricated as a 3-D model to evaluate vertical cell migration by confocal laser scanning microscopy and image processing.

Human skeletal muscle myoblasts (HSMMs; Lot. No. 4F1618; Lonza Walkersville Inc., Walkersville, MD, USA) and human dermal fibroblasts (HDFs; Lot. No. 6F4296; Lonza Walkersville Inc.) were used in the experiments. According to procedures described elsewhere (5, 8), the subcultures of HSMMs on laminin-coated surfaces were carried out at 37°C in an atmosphere of 5% CO_2 in Dulbecco's modified Eagle's medium (DMEM; Sigma-Aldrich, St. Louis, MO, USA) containing 10% fetal bovine serum (FBS; Invitrogen, Grand Island, NY, USA) and antibiotics (100 U/cm^3 penicillin G, 0.1 mg/cm^3 streptomycin, and 0.25 mg/cm^3 amphotericin B; Invitrogen).

As shown in Fig. 1A, starter cells harvested from the subcultures were stained using CellTracker Green™ and CellTracker Orange™ (Invitrogen) to exhibit fluorescently green and orange cells, respectively, according to commercially recommended protocol (5 μM for 15 min for live cell imaging). The stained cells were employed in the fabrication of the multilayered sheet according to newly developed procedures as follows. HSMMs were seeded at 2.3×10^5 cells/cm^2 in each well (diameter, 1.9 cm^2) of 24-well UpCell™ plates (CellSeed, Tokyo) with a temperature-responsive surface grafted with PIPAAm and incubated for 24 h at 37°C in 5% CO_2 to form the monolayer sheet. The medium depth was set to 2 mm throughout the experiments and HDFs were mixed into the sheet if needed. For stacking monolayer cell sheets to form the multilayered cell sheet, a manipulator was designed as shown in Fig. 1B composed of a stamp, its stand, and a mold to load the stamp with the gelatin gel. A solution of 7.4% gelatin was prepared by dissolving gelatin powder (G1890-100G; Sigma-Aldrich) in 5 mL Hank's balance salt solution (Sigma-Aldrich) and 100 μL of 1 N NaOH solution at 45°C for 30 min. The solution was then sterilized by filtration through a 0.22-μm filter (Millex-GS; Millipore Co., Billerica, MA, USA) and poured into the silicone molds under aseptic conditions. The stamps were put onto the molds on ice to gelation. Finally, the molds were gently removed and the stamps with the gelatin were ready to be used to stack the cell sheets. To harvest the monolayer sheet, the stamp with the gelatin gel was overlaid on the monolayer sheet in a well at 37°C and the temperature was shifted to 20°C (Fig. 1A). After 30 min, the stamp was lifted together with the monolayer sheet from the bottom surface of the well. The steps were

* Corresponding author. Tel.: +81 6 6879 7444; fax: +81 6 6879 4246.
E-mail address: kino-oka@bio.eng.osaka-u.ac.jp (M. Kino-oka).

1389-1723/$ - see front matter © 2011, The Society for Biotechnology, Japan. All rights reserved.
doi:10.1016/j.jbiosc.2011.09.001

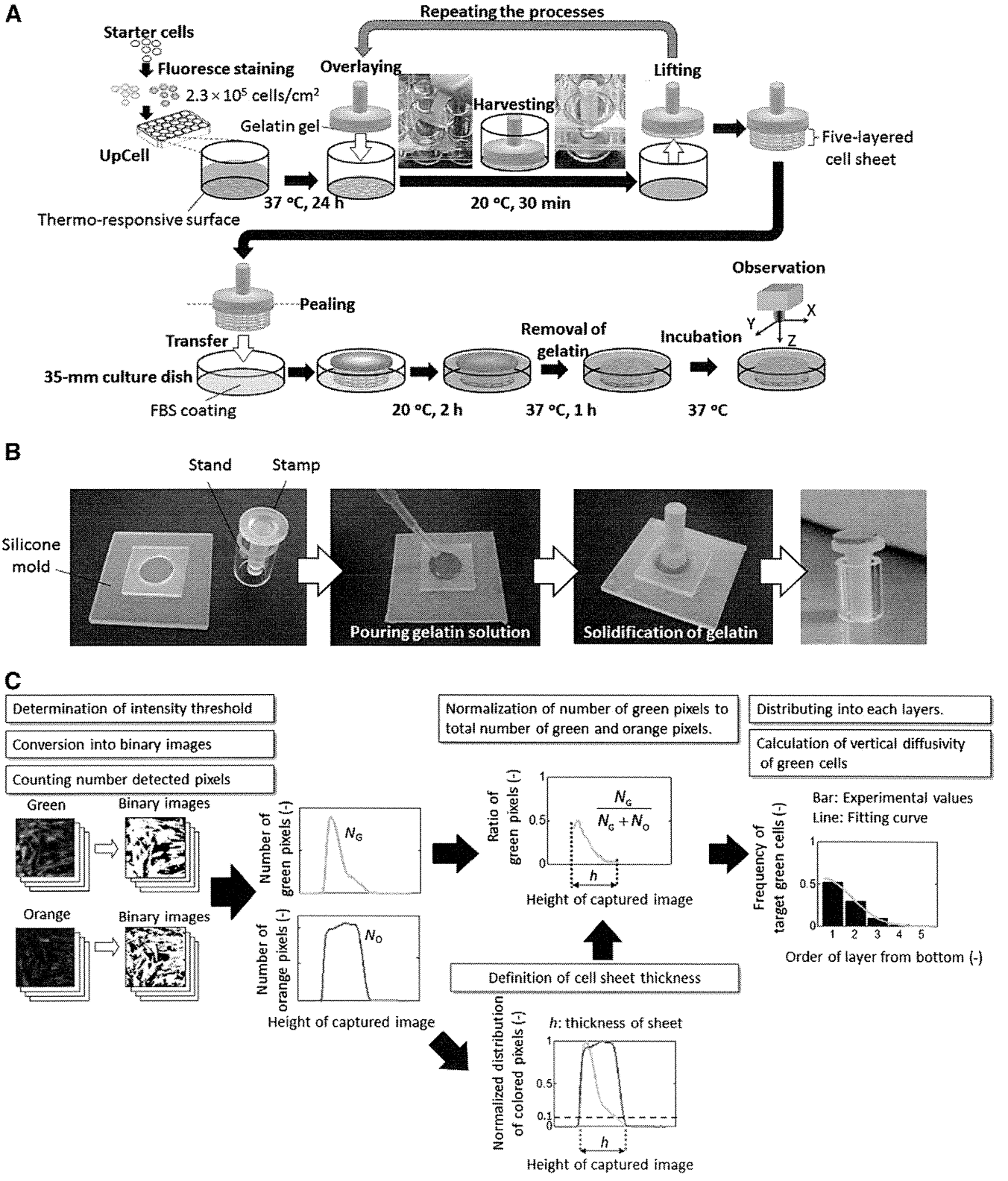

FIG. 1. Schematic diagrams showing the five-layered cell sheet fabrication and quantitative diffusivity analysis. (A) Fabrication of the five-layered cell sheet. (B) Preparation of the manipulator used to harvest the cell sheet. (C) Image processing system calculating the spatial distribution and diffusivity of the green target cells.

then repeated for the sequential harvests of monolayer sheets to form the multilayer structure on the stamp. The multilayered sheet with the gelatin was separated from the stamp and placed on a 35-mm culture dish (ibidi GmbH, Martinsried, Germany) that was precoated with 0.2 mL/cm^2 FBS for 24 h for the facilitation of the sheet attachment to the surface, and the dish was incubated for 2 h at 20°C in 5% CO_2 without the addition of medium. To remove gelatin, the medium (0.4 mL/cm^2) was added, and the temperature was

shifted to 37°C for 1 h to melt the gelatin and the medium was changed with a fresh one. In the present study, the fabricated culture system of a five-layered sheet was used to analyze sheet behaviors.

As a typical culture system, the five-layered sheet consisting of basal layers (green) and other layers (orange) stained by CellTracker Green™ and CellTracker Orange™, respectively, was prepared for the observation of tempo-spatial cell distribution using confocal laser scanning microscopes (FV10i for time lapse and FV-300 for spatial distribution; Olympus, Tokyo) with 60× objective lens. To determine the spatial distribution of the target cells, the green and orange cells in each layer at 0 and 48 h of incubation were observed and quantitatively analyzed using image processing (Fig. 1C). The five-layered sheet was washed twice with phosphate buffered saline (PBS) and then fixed with 4% paraformaldehyde in PBS (Wako Pure Chemical Industries, Osaka) overnight. After washing with PBS, at least eight random positions of each sample were scanned at a 0.6-μm interval to yield slice images for vertical direction determination. After intensity threshold values were identified, 8-bit images (256×256 pixels) of both colors in each slice were converted into binary images, leading to the distinction between colored and non colored pixels. Here the colored pixels which were derived from green and orange fluorescent original images denoted the green and orange pixels, respectively. The number of colored pixels in each slice was counted. The green and orange pixels in each slice were normalized using the maximum green and orange pixel values, respectively, found in all of the slice images. The slice possessing more than 10 % of the colored pixels was regarded to exist inside cell sheet, from which the vertical positions at top and bottom of the five-layered sheet, and the sheet thickness, h, were determined. The ratio of green pixels to sum of green and orange pixels in each slice was normalized to determine the distribution of green pixels by dividing into 5 layers. Here, the normalized distribution of green pixels was assumed to be equivalent to the green cell distribution in the sheet, recorded by the frequency of green cells, f_G, in each layer.

Time-lapse observation was conducted of the five-layered sheet (Supplementary Movie S1). During the early incubation period, the green cells were observed in the bottom of the sheet, and the active cellular migration occurred in the horizontal and vertical directions anywhere in the sheet, revealing the sheet fluidity. The green cells then migrated toward the upper layers as time elapsed. To understand the extent of the sheet fluidity, the vertical distribution of green cells was estimated. Figure 2 shows the histograms of f_G at 0 and 48 h. The f_G values in the first and second layers from the bottom surface were estimated to be $f_G = 0.82$ and 0.17, respectively, and the sheet at 48 h had a broad distribution of f_G, being $f_G = 0.37$ in the first layer. In addition, the f_G decreased gradually along the layers from bottom to top, suggesting the analogy of vertical migration to molecular diffusion. To quantitatively analyze vertical sheet fluidity, the diffusivity, D, was determined based on Fick's second law, $\frac{\partial f_G}{\partial t} = D\frac{\partial^2 f_G}{\partial h^2}$, in which f_G, t, and h represent the green cell frequency, incubation time, and sheet thickness, respectively. The Crank–Nicolson finite difference method and least squares method were applied to calculate the diffusivity using a custom-made software programmed by LabVIEW (National Instruments, Austin, TX, USA). The initial condition was that the total ratio of green cells in the five layers was normalized to unity. The free boundary condition, $\frac{df_G}{dh} = 0$, is set at both the bottom and the top of the five-layered sheet. In a practical aspect, the f_G distribution data at 0 and 48 h were applied to calculate the apparent vertical diffusivity of green cells, $\bar{D}_0$, being $\bar{D}_0 = 0.74\ \mu m^2/h$ (Table 1).

To investigate sheet fluidity variation, we incubated five-layered sheets added with HDFs comprising 25% and 50% of the cell counts (conditions B and C, respectively). As shown in Table 1, the $\bar{D}_0$ increased at 25% addition (condition B) compared to that without any HDF addition (condition A), although the significance level was not sufficient ($p<0.06$). In addition, 50% addition (condition C) caused a decrease in $\bar{D}_0$ compared to that at 25% addition ($p<0.05$). For further understanding of the role of HDFs addition, we established the five-layered sheet system composed of HSMMs or HDFs in basal layer stained by CellTracker Green™ and the rest of cells stained by CellTracker Orange™, and estimated the diffusivity of basal HSMMs or HDFs, $\bar{D}_M$ or $\bar{D}_F$, respectively (Table 1). At 25% addition, $\bar{D}_F$ was estimated to be $2.40\ \mu m^2/h$, being 4 times larger than $\bar{D}_M$. At 50% addition, $\bar{D}_F$ decreased to $0.80\ \mu m^2/h$, although $\bar{D}_M$ stayed constant, suggesting that $\bar{D}_0$ depended on HDF migration in the sheet.

An independent experiment showed that the migration rate of single HDF is 1.5 times higher than that of single HSMMs in culture using a conventional T-flask (data not shown). Pittet et al. reported that HDFs exhibited strong OB-cadherin connection in high-density culture (9). These results suggest that HDF active migration physically facilitated the overall fluidity in the sheet at lower HDF addition levels. It is most likely that higher HDF addition induced strong HDF intracellular binding in the sheet, and this strong interaction with lower HDF migration rates resulted in the decline of overall sheet fluidity.

The inner structural fluidity of cells in 3-D constructs has been reported in cultured neurospheres (10) and embryoid bodies (11). In static suspension cultures of mouse neural stem cells, active migration of single cells caused aggregate formation through intercellular coalescence, and culture prolongation led to cell division in the aggregates as well as accidental coalescence between independent aggregates that formed large spheres in which the location of distribution of differentiated neurons and glia was observed (12). Further observation revealed that the large sphere was caused by spontaneous active migration in aggregates through the live-cell imaging technique. In addition, Duguay et al. (13) reported that aggregation using a mixture of E-cad-expressing E8a cell line and P-cad-expressing LP1 cell line caused spatial habitant isolation of 3-D spheres via active cell migration and intercellular binding affinity, leading to autonomous double-layer spheres by different cell types. These results mean the importance of cell migration in 3-D constructs

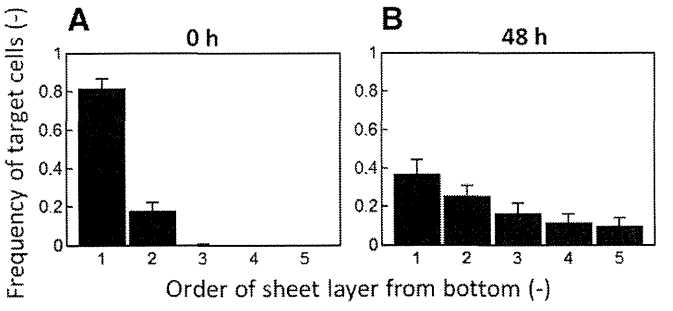

FIG. 2. Spatial distributions of the green target cells inside the cell sheet at 0 (A) and 48 h (B). Bars show the standard deviation (SD) ($n=3$).

TABLE 1. Diffusivities of different target cells from the basal layer in the five-layered cell sheet at different cellular balance conditions.

Condition	HSMMs (%)	HDFs (%)	Initial thickness of sheet, h (μm)	Diffusivity (μm²/h)		
				$\bar{D}_0$	$\bar{D}_M$	$\bar{D}_F$
A	100	0	33.0±5.4	0.74±0.23	–	–
B	75	25	36.4±5.4	1.57±0.50	0.57±0.14	2.40±0.49
C	50	50	37.7±5.0	0.69±0.12	0.54±0.26	0.80±0.36

$\bar{D}_0$, $\bar{D}_M$, and $\bar{D}_F$ are the diffusivities of whole cells, skeletal myoblasts, and dermal fibroblasts from the basal layer, respectively. HSMMs, human skeletal muscle myoblasts; HDFs, human dermal fibroblasts. All values were expressed as mean±SD ($n=3$).

affecting the fate of stem cells as well as spatial habitant isolation of differentiated cells. In the current study, HDF addition was found to affect sheet fluidity. Further experiments clarified the localization of HDFs in five-layered sheets (Oda, M. et al., Abstr., 10th Congress of the Japanese Society for Regenerative Medicine, p. 248, 2011). This finding suggested that the cell sheet fabricated from HMMs and HDFs exhibited the habitant isolation between them.

Many researchers have paid much attention to tissue mimicry by using cellular aggregates, which are considered minimized functional structures. The mimic constructs have broad potential use as transplants in regenerative medicine as well as structural material for elucidating the dynamic tissue development mechanism. From the standpoint of analytical techniques, observational convenience of 3-D constructs is a critical requirement because cellular behaviors such as migration, division, and communication affect the common mechanisms of tissue development.

In conventional studies, most of the techniques for fabricating cell aggregates led to spherically shaped constructs through spontaneous formation by cellular coagulation. In contrast, the current system applied the plate shape of the multilayered sheet using artificially designed formation by the assembly of monolayer sheets because the mimic system using the plate-shaped aggregate has the observational advantage in the 3-D construct. The plate-shaped aggregates can be fabricated in various ways using cell sheet engineering technique with thermo-responsive polymer grafted surface (1), biodegradable peptide grafted surface (14) or collagenase degradable atelocollagen film (15), magnetic-force based tissue engineering technique (16), layer-by-layer assembly technique with ECM coating cells (17), compressed collagen sheet (18), vitrified collagen film "vitrigel" (19), and bioprinting method (20).

Our system that uses multilayered sheet containing stained target cells in the basal layer and confocal laser scanning microscopy realizes clear observation of target cell behaviors in the vertical direction, enabling monodimensional analysis of vertical cell distribution inside the sheet. The reduced spatial dimension makes easy to analyze cell migration, compared to the full 3-D analysis required of spherically shaped aggregates. Thus, the system developed in the present study can be a powerful tool for elucidating dynamic phenomena in 3-D constructs.

Supplementary data to this article can be found online at doi:10.1016/j.jbiosc.2011.09.001.

This study was supported by the New Energy and Industrial Technology Development Organization (NEDO) of Japan, and the Japan Society for the Promotion of Science (JSPS) through the "Funding Program for World-Leading Innovative R&D on Science and Technology (FIRST Program)," initiated by the Council for Science and Technology Policy (CSTP).

References

1. **Yang, J., Yamato, M., Kohno, C., Nishimoto, A., Sekine, H., Fukai, F., and Okano, T.:** Cell sheet engineering: recreating tissues without biodegradable scaffolds, Biomaterials, **26**, 6415–6422 (2005).
2. **Sasagawa, T., Shimizu, T., Sekiya, S., Haraguchi, Y., Yamato, M., Sawa, Y., and Okano, T.:** Design of prevascularized three-dimensional cell-dense tissues using a cell sheet stacking manipulation technology, Biomaterials, **31**, 1646–1654 (2010).
3. **Horwitz, R. and Webb, D.:** Cell migration, Curr. Biol., **13**, R756–R759 (2003).
4. **Louis, M., Zanou, N., Van, S. M., and Gailly, P.:** TRPC1 regulates skeletal myoblast migration and differentiation, J. Cell Sci., **121**, 3951–3959 (2008).
5. **Chowdhury, S. R., Muneyuki, Y., Takezawa, Y., Kino-oka, M., Saito, A., Sawa, Y., and Taya, M.:** Synergic stimulation of laminin and epidermal growth factor facilitates the myoblast growth through promoting migration, J. Biosci. Bioeng., **108**, 174–177 (2009).
6. **Wang, W., Pan, H. Y., Murray, K., Jefferson, B. S., and Li, Y.:** Matrix metalloproteinase-1 promotes muscle cell migration and differentiation, Am. J. Pathol., **174**, 541–549 (2009).
7. **Bondesen, B. A., Jones, K. A., Glasgow, W. C., and Pavlath, G. K.:** Inhibition of myoblast migration by prostacyclin is associated with enhanced cell fusion, FASEB J., **21**, 3338–3345 (2007).
8. **Chowdhury, S. R., Muneyuki, Y., Takezawa, Y., Kino-oka, M., Saito, A., Sawa, Y., and Taya, M.:** Growth and differentiation potentials in confluent state of culture of human skeletal muscle myoblasts, J. Biosci. Bioeng., **109**, 310–313 (2010).
9. **Pittet, P., Lee, K. M., Kulik, A. J., Meister, J. J., and Hinz, B.:** Fibrogenic fibroblasts increase intercellular adhesion strength by reinforcing individual OB-cadherin bonds, J. Cell Sci., **121**, 877–886 (2008).
10. **Singec, I., Knoth, R., Meyer, R. P., Maciaczyk, J., Volk, B., Nikkhah, G., Frotscher, M., and Snyder, E. Y.:** Defining the actual sensitivity and specificity of the neurosphere assay in stem cell biology, Nat. Methods, **3**, 801–806 (2006).
11. **Dang, S. M., Kyba, M., Perlingeiro, R., Daley, G. Q., and Zandstra, P. W.:** Efficiency of embryoid body formation and hematopoietic development from embryonic stem cells in different culture systems, Biotechnol. Bioeng., **78**, 442–453 (2002).
12. **Mori, H., Ninomiya, K., Kanemura, Y., Yamasaki, M., Kino-oka, M., and Taya, M.:** Image cytometry for analyzing regional distribution of cells inside human neurospheres, J. Biosci. Bioeng., **103**, 384–387 (2007).
13. **Duguay, D., Foty, R. A., and Steinberg, M. S.:** Cadherin-mediated cell adhesion and tissue segregation: qualitative and quantitative determinants, Dev. Biol., **253**, 309–323 (2003).
14. **Qiu, F., Chen, Y., Cheng, J., Wang, C., Xu, H., and Zhao, X.:** A simple method for cell sheet fabrication using mica surfaces grafted with peptide detergent A(6)K, Macromol. Biosci., **10**, 881–886 (2010).
15. **Nagai, N., Yunoki, S., Satoh, Y., Tajima, K., and Munekata, M.:** A method of cell-sheet preparation using collagenase digestion of salmon atelocollagen fibrillar gel, J. Biosci. Bioeng., **98**, 493–496 (2004).
16. **Ito, A., Shinkai, M., Honda, H., and Kobayashi, T.:** Medical application of functionalized magnetic nanoparticles, J. Biosci. Bioeng., **100**, 1–11 (2005).
17. **Matsusaki, M., Kadowaki, K., Nakahara, Y., and Akashi, M.:** Fabrication of cellular multilayers with nanometer-sized extracellular matrix films, Angew. Chem. Int. Ed., **46**, 4689–4692 (2007).
18. **Brown, R. A., Wiseman, M., Chuo, C. B., Cheema, U., and Nazhat, S. N.:** Ultrarapid engineering of biomimetic materials and tissues: fabrication of nano- and microstructures by plastic compression, Adv. Funct. Mater., **15**, 1762–1770 (2005).
19. **Takezawa, T., Ozaki, K., Nitani, A., Takabayashi, C., and Shimo-Oka, T.:** Collagen vitrigel: a novel scaffold that can facilitate a three-dimensional culture for reconstructing organoids, Cell Transplant., **13**, 463–473 (2004).
20. **Nakamura, M., Iwanaga, S., Henmi, C., Arai, K., and Nishiyama, Y.:** Biomatrices and biomaterials for future developments of bioprinting and biofabrication, Biofabrication, **2**, 014110 (2010).

Mol Cell Biochem (2012) 368:203–214
DOI 10.1007/s11010-012-1361-4

Transplantation of elastin-secreting myoblast sheets improves cardiac function in infarcted rat heart

Ayako Uchinaka · Naomasa Kawaguchi · Yoshinosuke Hamada · Shigeru Miyagawa · Atsuhiro Saito · Seiji Mori · Yoshiki Sawa · Nariaki Matsuura

Received: 15 February 2012 / Accepted: 7 June 2012 / Published online: 21 June 2012

Abstract Myoblast sheet transplantation for cardiac failure is a promising therapy to enhance cardiac function via paracrine mechanism. However, their efficacies of treatment showed a gradual decline. The gene modification of the implanted myoblast is important in improving the long-term results of the treatment. Elastin fiber enhances the extensibility of the infarcted wall and can prevent left ventricular dilation. We therefore hypothesized that the elastin gene modification of the implanted myoblast could strengthen and maintain the long-term improvement effects of cardiac function. In this study, we evaluated long-term follow-up benefits of functional myoblast sheets that secrete elastin in an infarcted model. The animal models were divided into three groups: a group transplanted with nontransfected, wild-type, skeletal myoblast-type sheets (WT-rSkM); group transplanted with myoblast sheets that secreted elastin fragments (ELN-rSkM); and a control group (ligation only). Cardiac function was examined by echocardiography, and cardiac remodeling after infarction was evaluated by histological examination. The cardiac function was significantly improved and the left ventricle end-diastolic dimensions were significantly reduced in the ELN-rSkM group. Histological analysis showed that left ventricular remodeling was attenuated in the ELN-rSkM group and that elastic fiber was formed in the epicardial area of ELN-rSkM group. The functionalization of myoblast sheet by elastin gene transfer showed the long-term improvement of cardiac function. Expressed recombinant elastin fiber prevented the dilation of the left ventricular chamber after myocardial infarction. The functional myoblast sheet transplantation maintained the treatment effect by the paracrine effect of myoblast and the formed recombinant elastin.

Keywords Myocardial infarction · Cell transplantation · Remodeling · Elastin · Gene expression

A. Uchinaka · N. Kawaguchi (✉) · Y. Hamada · S. Mori · N. Matsuura
Department of Molecular pathology, Osaka University Graduate School of Medicine, Division of Health Sciences, 1-7 Yamada-oka, Suita, Osaka 565-0871, Japan
e-mail: kawaguch@sahs.med.osaka-u.ac.jp

S. Miyagawa · Y. Sawa
Department of Cardiovascular Surgery, Osaka University Graduate School of Medicine, Suita, Japan

A. Saito
Medical Center of Translational Research, Osaka University Graduate School of Medicine, Suita, Japan

Introduction

In recent years, myocardial regeneration therapy using cell transplantation has been examined for the treatment of heart failure [1–3]. In the several cell sources such as smooth muscle cells and bone marrow-derived cells, transplantation of skeletal myoblasts have achieved better therapeutic effects [4–6]. The therapeutic effect of the myoblast sheet is considered to be mediated by the production of paracrine effectors that locally stimulate the injured myocardium [7, 8]. However, autologous skeletal myoblast transplantation by means of the injection method has some disadvantages, including the loss of transplanted cells, inadequate survival of grafted cells, and arrhythmogenicity [9, 10]. We therefore investigated a novel cell transplantation technique using cell sheets grown in temperature-responsive dishes [8, 11] as a means of overcoming these problems. We have previously shown that transplantation of autologous skeletal myoblast sheets is

superior to direct myocardial injection in cell therapy of heart failure in studies on both small and large animals [12–14]. Furthermore, beneficial results of the implantation of a layered myoblast sheet in comparison with a single-layered sheet included a greater improvement in cardiac function, fewer fibrosis, and less hypertrophy [15].And, when layered myoblast sheets were transplanted onto the infarcted area, the amount of elastic fiber increased in the implanted area with expression of tropoelastin mRNA. The relative expression of rat tropoelastin mRNA increased in a dose-dependent fashion [15]. We therefore hypothesize that the expression of elastin is a contributory factor in the therapeutic effects of myoblast sheets and that the overexpression of elastin could strengthen these effects.

When we followed up the cardiac function after myoblast sheet transplantation until 8 weeks after sheet transplantation, the efficacies of the sheet transplantation showed a gradual decline. The modification of the implanted myoblast is very important in improving the long-term results of the treatment. In curing cardiac disease, the necrotic myocardium is replaced by collagen fiber, and elasticity is lost in the scarred area. As a result, the diastolic performance of the left ventricle (LV) declines with time [16, 17]. Therefore, we hypothesized that elastin secreted from the implanted myoblast sheets might generate elasticity in the infarcted area. Additionally, by transplantation of the sheets to the epicardium, we hoped that a layer of elastic fiber would be formed and inhibit dilatation of the LV chamber, conferring a guard ring effect. Because the lifespan of elastin fibers is in the region of years, the cardiac function might be stabilized in the long term. At present, myocardial regeneration therapy using cell transplantation combined with elastin is hardly ever performed in the case of serious heart failure, and approaches to therapy of cardiac disease with elastin have not been reported besides the reports by Mizuno et al. Mizuno and co-workers reported that injection of elastin gene-transfected COS7 cells into an infarcted heart improved its performance[18, 19]. The COS7 cell is an endothelial cell from the African green monkey kidney, and endothelial cells alone do not improve the function of the LV after myocardial damage. Because we used myoblasts, which can themselves affect cardiac function and remodeling, additional therapeutic effects might be expected. We have expected that the paracrine function by myoblast will have a curative effect in the early stage, and the guard ring function of the recombinant elastin will inhibit the LV chamber dilation in the late stage.

In the present study, we constructed functional skeletal myoblast sheets that secrete elastin and examined their effects in improving cardiac function and the remodeling in rats with myocardial infarction (MI).

Materials and methods

Isolation of skeletal myoblasts

Myoblasts were isolated from the skeletal muscle of the tibialis anterior from three-week-old male Lewis rats. After the removal of connective tissues, such as tendons and fibrous tissue, the muscles were minced and enzymatically dissociated with 0.2 % collagenase type II (Worthington Biochemical Corp., Lakewood, NJ, USA) and trypsin for 30 min at 37 °C. The enzymatic reaction was arrested by addition of Dulbecco's modified Eagle's medium (DMEM) (Nihonseiyaku, Tokyo, Japan) containing 20 % fetal bovine serum (FBS) (Biowest, Miami, FL, USA), and the cells were collected by centrifugation. The cells were suspended in culture medium composed of DMEM with 20 % FBS and 1 % antibiotic–antimycotic solution (Invitrogen Life Technologies). After being pre-plated twice, nonadherent cells were then plated on a Matrigel (Becton–Dickinson Bioscience)-coated dish and incubated at 37 °C, 5 % CO_2. The purity of the culture was evaluated by immunofluorescence imaging. The isolated cells fixed with 4 % paraformaldehyde were incubated with anti-desmin antibody (Sigma, St. Louis, MO, USA) and followed by incubation with fluorescein isothiocyanate [FITC; 2-(3,6-dihydroxy-9H-xanthen-9-yl)-5-isothiocyanato-benzoic acid] conjugated anti-rabbit secondary antibody (GE Healthcare, Piscataway, NJ, USA). The nuclei were stained with 4′,6-diamino-2-phenylindole (DAPI; Invitrogen Life Technologies) and the fluorescent signals were detected by fluorescence microscopy (ECLIPSE E600, Nikon, Tokyo, Japan).

Animal ethics

This animal experiment was approved by the Animal Care Committee of Osaka University graduate school of medicine. Humane animal care was used in compliance with the Principals of Laboratory Animal Care formulated by the National Society for Medical Research, and the Guide for the Care and Use of Laboratory Animals prepared by the Institute of Laboratory Animal Resource and published by the National Institute of Health (NIH publication No.85–23, revised 1996).

Animal model

Eight-week old female F344/NJcl-rnu/rnu rats were used as recipients. The rats were anesthetized with isoflurane (2 %, 0.2 ml/min) by inhalation. They were then intubated, and respirator served to maintain ventilation during surgery. The adequacy of anesthesia was monitored by electrocardiogram and pulse rate. MI was produced by ligation of the

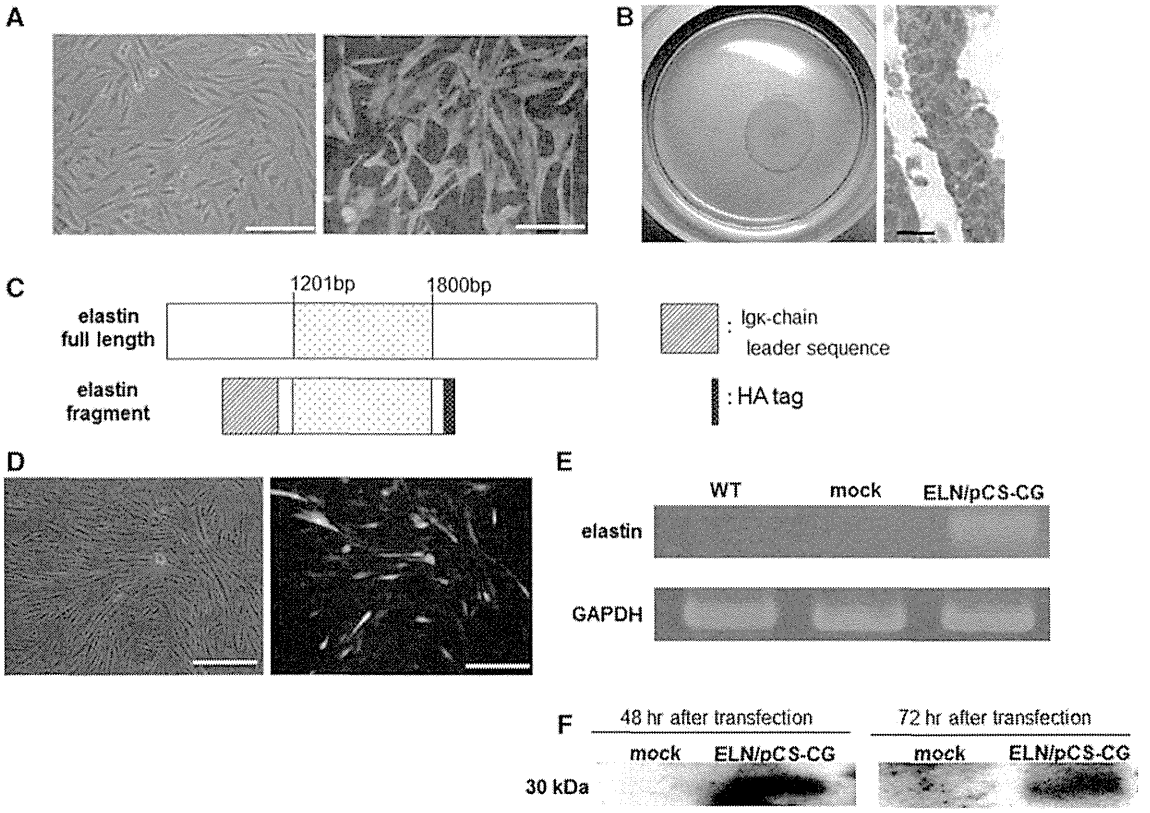

Fig. 1 Characteristics of isolated myoblasts and expression of elastin in isolated myoblasts. **a** Isolated skeletal myoblasts (passage 2) (*left-hand side*) and its immunofluorescent staining (*right-hand side*) (*green* desmin, *blue* nucleus *scale bar* 100 μm). High-purity skeletal myoblasts can therefore be isolated. **b** The rat skeletal myoblast (rSkM) sheet (*left*). Staining by hematoxylin and eosin of a cross section of the rSkM sheet (*right*, *scale bar* 50 μm). **c** View showing the frame format of the constructed rat tropoelastin gene. **d** Determination of lentiviral transduction efficiency (*scale bar* 100 μm). **e**, **f** Assessment of expression of the recombinant elastin by RT-PCR and western blotting. The secreted recombinant elastin protein was detected in the culture medium of rSkM cells infected with ELN/pCS-CG, whereas no elastin expression was detected in control cells

left anterior descending coronary artery (LAD). When the baseline cardiac function was measured by echocardiography two weeks after the ligation, we monitored the depression of the left ventricular anterior wall movement. And, at the time of sheet transplantation, we macroscopically confirmed the scar area which spread from ligated portion toward cardiac apex, and implanted the myoblast sheets on the scar region without use of suture. The rats were divided into three groups: (1) a WT-rSkM group (implanted with three nontransfected wild-type myoblast sheets, $n = 6$), (2) an ELN-rSkM group (implanted with three myoblast sheets that secreted elastin fragments, $n = 8$), and (3) a control group (re-opened the chest at 2 weeks when other two groups were implanted with myoblast sheets, $n = 6$). The implanted sheets adhere to myocardium immediately and don't fall off after closing the chest because the cell sheets maintain the cell–cell and cell-extracellular matrix (ECM) adhesion. After detachment from the temperature-responsive dish, each sheet was picked up individually and applied to surface of the heart. So that the sheet could be spread, the folded areas were gently stoked with wet, round tip forceps. After confirmation of the adherence of the implanted sheets, subsequent sheets were applied by the same technique.

Elastin overexpression and transfection

Lentiviral vector which includes the cDNA of the fragment (from 1,201 to 1,800 bp) of rat tropoelastin (ELN/pCS-CG) was constructed (Fig. 1c). And the isolated rSkM were transfected with incubation for 48 h in the presence of ELN/pCS-CG and 8 μg/ml polybrene (Sigma). Expression of the recombinant elastin gene was examined by RT-PCR and Western blotting after 5 days.

Reverse transcription-polymerase chain reaction assay

After 5 days of transduction, the cells were lysed with Sepasol (Nacalai Tesque, Kyoto, Japan), and the total RNA was isolated. Glyceraldehyde 3-phosphate dehydrogenase (GAPDH) was used as an internal control.

The following primer sequences were used for PCR: elastin fragment (333 bp): 5′-GGTGCACTGCCAGGTGC AGTACCA-3′ (forward) and 5′-AGCGTAATCTGGAAC ATCGTATGG-3′ (reverse) rat GAPDH (393 bp): 5′-ACT GGCGTCTTCACCACCAT-3′ (forward) and 5′-AGTGA GCTTCCCGTTCAGCT-3′(reverse)

Western blotting assay

The culture medium was collected and centrifuged, and supernatants were used for the assays. Each sample was subjected to electrophoresis on polyacrylamide gels and then electro transferred to a polyvinylidene fluoride transfer membrane (Millipore, Billerica, MA, USA). After blocking (5 % nonfat milk), the membrane was probed with a primary antibody against HA tag (Santa Cruz Biotechnology, California, USA). The membranes were incubated with anti-rabbit IgG-linked horseradish peroxidase (GE Health care) and then exposed to SuperSignal West Femto (Thermo Fisher Scientific Inc, Waltham, MA, USA).

Sheet production

Four days after lentivirus transduction, 3×10^6 infected myoblasts were placed on a 35-mm temperature-responsive culture dish (UpCell; Cellsheed, Tokyo, Japan) and incubated. After 16 h, the cell sheets were detached at room temperature for 30 min (Fig. 1b).

Measurement of cardiac function

The cardiac function of the treated rats was monitored by echocardiography 2, 4, 6, and 8 weeks after sheet implantation. The measurements were performed by using a SONOS 5500 sonograph (Agilent Technologies, Palo Alto, Calif) with a 12-MHz transducer. The rats were anesthetized with isoflurane (2 %, 0.2 ml/min) by inhalation, as mentioned above. The hearts were visualized as short-axis two-dimensional images at the level of the papillary muscles. The LV-end systolic area, the LV-end diastolic area, and the LV dimensions at end-systole and end-diastole (LVIDd and LVIDs, respectively) were determined. On the basis of these results, the ejection fraction (EF), fractional shortening (FS), end-diastolic volume (EDV), and end-systolic volume (ESV) were calculated as follows.

(1) $\text{LVEF}\ (\%) = (\text{LVDd}^3 - \text{LVDs}^3)/\text{LVDd}^3 \times 100\ (\%)$.
(2) $\text{LV}\ \%\ \text{FS} = [(\text{LVDd} - \text{LVDs})/\text{LVDd}] \times 100\ (\%)$.
(3) $\text{EDV} = \text{LVIDd}^3 \times (0.98 \times \text{LVIDd} + 5.90)\ (\text{ml})$.
(4) $\text{ESV} = \text{LVIDs}^3 \times (1.14 \times \text{LVIDs} + 4.18)\ (\text{ml})$.

Heart weight/body weight ratio

The rats' body weights were measured 8 weeks after sheet transplantation. And then, the rats were anesthetized with intraperitoneal pentobarbital (300 mg/kg) and heparin (150 U), and their hearts were rapidly removed. The weights of the removed hearts were also measured and the ratio of the heart weight (mg) to the body weight (g) (HW/BW) was calculated.

Histological analyses

LV myocardium species were obtained 8 weeks after sheet implantation. The fixed sample was embedded in paraffin. The LV chamber diameter and the anterior wall thickness were measured for sections stained with Hematoxylin–Eosin (HE). Infarcted wall thickness, posterior wall thickness, and LV chamber diameter were measured with the scale loupe. Sirius red stain was used to detect the fibrosis. The fibrosis was evaluated from the fibrotic ratio in the infarct border region at a magnification of 200×. Periodic acid–Schiff staining for cardiomyocyte hypertrophy was also performed. Cardiomyocytes ($n = 100$) at 400× magnification were randomly selected in border and remote area of the infarct, and their minor axes across the nucleus were measured. To label vascular endothelial cells so that blood vessels could be counted, we performed immunohistochemical staining for Von Willebrand factor antigen. Paraffin sections were deparaffinized in xylene, dehydrated in graded ethanol mixtures, and processed for antigen retrieval by autoclaving in 0.01-M citrate buffer. Endogenous peroxidase was blocked by immersing the sections in methanol containing 3 % hydrogen peroxide. After blocking with 5 % BSA, the sections were incubated with primary antibody against Von Willebrand Factor (rabbit-polyclonal; DAKO, Glostrup, Denmark). The sections were incubated with a biotinylated anti-rabbit IgG antibody (DAKO) and further incubated with a peroxidase-conjugated streptavidin (GE Health Care). Visualization was performed using biphenyl-3,3′,4,4′-tetramine (DAB) solution (Sigma). Twenty different fields at 400× magnification were randomly selected, and the number of the stained vascular endothelial cells in each field was counted under a light microscope. The distribution of elastin fibers was evaluated by means of Victoria blue-HE staining or elastica van Gieson staining.

Expression of elastin and matrix metalloproteinase in myocardial tissue

The samples of myocardial tissue removed 8 weeks after sheet transplantation were divided into infarction, border, and remote areas. Each sample was homogenized in SDS

buffer and centrifuged, and the supernatants were used for assays by Western blotting, as previously described. The primary antibodies used were rabbit polyclonal anti-elastin (Acris Antibodies GmbH, Herford, Germany), rabbit polyclonal anti-matrix metalloproteinase 1 (anti-MMP-1) (LifeSpan Biosciences Inc., Seattle, WA, USA), mouse monoclonal anti-matrix metalloproteinase 2 (anti-MMP-2) (Daiichi Fine Chemical Co., Ltd., Toyama, Japan), and mouse monoclonal anti-muscle actin (Dako). We quantified the density of the bands of elastin, MMP-1, and MMP-2 using α-tubulin of each lane as a standard.

Statistical analyses

Data are presented as the mean ± standard error of mean (SEM). The cardiac function was analyzed by repeated measurement ANOVA for differences across the whole time course and one-way ANOVA, whereas the Tukey–Kramer post hoc test was used to examine for significant differences at each time point.

To assess the significance of the differences between individual groups for other data, statistical comparisons were performed by an unpaired Student's t test. A value of $P < 0.05$ was considered statistically significant.

Results

Isolation of rat skeletal myoblasts

To confirm that the isolated cells from the skeletal muscle were myoblasts, we performed immunofluorescent staining with anti-Desmin antibody. Fluorescence microscopy studies showed that more than 80 % of the isolated cells were desmin-positive (Fig. 1a). High-purity skeletal myoblasts can therefore be isolated.

mRNA expression and elastin secretion in rat skeletal myoblasts

The efficiency of infection of the rSkM was >70 % (Fig. 1d). The expression of elastin mRNA was recognized in rSkM infected with ELN/pCS-CG (Fig. 1e), whereas expression of elastin was not detected in noninfected rSkM (WT) or control cells infected with the empty vector (mock). The secreted recombinant elastin protein was detected in the culture medium of rSkM cells infected with ELN/pCS-CG, whereas no elastin expression was detected in the control cells (Fig. 1f).

Elastin-expressing myoblast sheets enhance ventricular function after MI

There was no difference in echocardiographic parameters such as LVEF or %FS between the groups before sheet transplantation. Echocardiography showed a significant improvement in LVEF and %FS in the WT-rSkM and ELN-rSkM groups in comparison with the control group 2, 4, 6, or 8 weeks after implantation ($P < 0.01$). In addition, the values of LVEF and %FS in the ELN-rSkM group 2, 6, and 8 weeks after implantation were significantly improved in comparison with that of the WT-rSkM group (2 and 6 weeks; $P < 0.05$; 8 weeks; $P < 0.01$) (Figs. 2a, b).

The evaluation of LVIDd and LVIDs over time showed the inhibition of dilation in all measure points in the ELN-rSkM group relative to the control and WT-rSkM groups. And, especially at late points, 6 and 8 weeks after implantation, they were significantly attenuated in the ELN-rSkM group compared with the control group (LVIDd: 8 weeks $P < 0.05$, LVIDs: 6 weeks $P < 0.05$, 8 weeks $P < 0.01$) (Table 1). The values of EDV and ESV in the ELN-rSkM group were also smaller than the control and WT-rSkM groups in all measure points. The

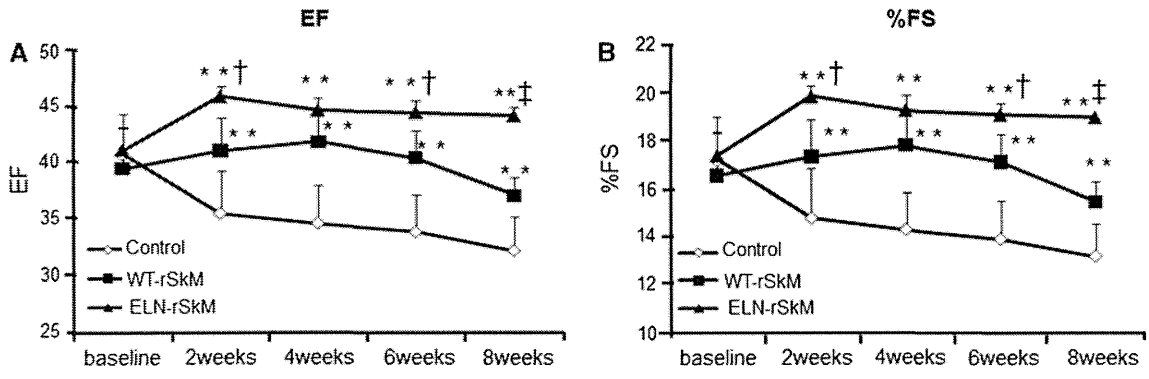

Fig. 2 Left ventricular function after myoblast sheet transplantation by echocardiography (**a** *EF* ejection fraction, **b** *% FS* % fractional shortening) Echocardiography showed a significant improvement in LVEF and % FS in the WT-rSkM and ELN-rSkM groups in comparison with the control group 2, 4, 6, or 8 weeks after implantation. In addition, the values of LVEF and %FS in the ELN-rSkM group 2, 6, and 8 weeks after implantation were significantly improved in comparison with that of the WT-rSkM group $^{**}P < 0.01$ versus control. $\dagger P < 0.05$, $\ddagger P < 0.01$ versus WT-rSkM

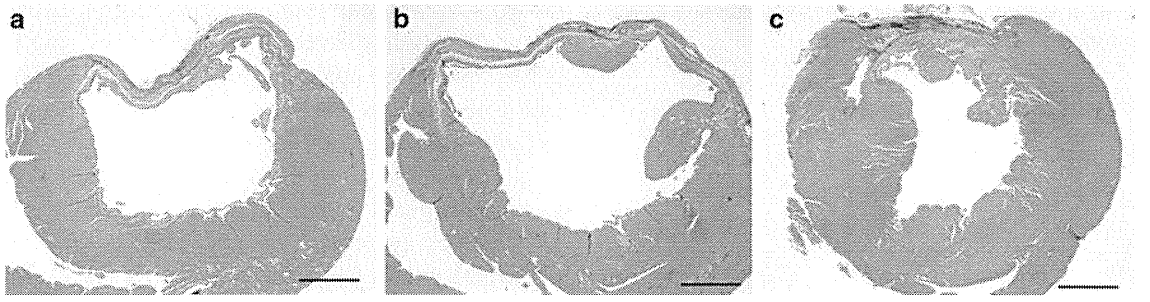

Fig. 3 Victoria blue-HE stained section of LV **a** control, **b** WT-rSkM, **c** ELN-rSkM (×10, *scale bar* 1,000 μm, *blue*: elastic fiber). The occurrence of thinning of the infarcted wall in the control group and the WT-rSkM group, whereas its thickness was maintained in the ELN-rSkM group

Table 1 The assessments of LVIDd, LVIDs, EDV, and ESV over time by echocardiography

	Baseline	2 weeks	4 weeks	6 weeks	8 weeks
LVIDd					
Control	0.73 ± 0.08	0.77 ± 0.07	0.81 ± 0.05	0.86 ± 0.05	0.88 ± 0.04
WT-rSkM	0.72 ± 0.08	0.77 ± 0.03	0.79 ± 0.04	0.83 ± 0.05	0.85 ± 0.04
ELN-rSkM	0.71 ± 0.09	0.73 ± 0.08	0.77 ± 0.06	0.80 ± 0.05	0.80 ± 0.06*
LVIDs					
Control	0.60 ± 0.06	0.65 ± 0.06	0.69 ± 0.04	0.74 ± 0.05	0.76 ± 0.04
WT-rSkM	0.61 ± 0.07	0.63 ± 0.03	0.67 ± 0.05	0.70 ± 0.04	0.72 ± 0.03
ELN-rSkM	0.59 ± 0.07	0.59 ± 0.07	0.63 ± 0.05	0.67 ± 0.05*	0.67 ± 0.06**
EDV					
Control	2.60 ± 0.78	3.05 ± 0.91	3.59 ± 0.66	4.29 ± 0.70	4.57 ± 0.59
WT-rSkM	2.54 ± 0.74	3.11 ± 0.32	3.33 ± 0.54	3.86 ± 0.71	4.07 ± 0.61
ELN-rSkM	2.45 ± 0.84	2.68 ± 0.92	3.19 ± 0.74	3.48 ± 0.73	3.50 ± 0.86*
ESV					
Control	1.07 ± 0.30	1.40 ± 0.38	1.67 ± 0.31	2.06 ± 0.44	2.23 ± 0.35
WT-rSkM	1.13 ± 0.32	1.25 ± 0.16	1.50 ± 0.34	1.69 ± 0.30	1.86 ± 0.26
ELN-rSkM	1.01 ± 0.35	1.01 ± 0.37	1.26 ± 0.30	1.49 ± 0.33*	1.50 ± 0.32**

* $P < 0.05$, ** $P < 0.01$ versus control of each measure point

enlargement of EDV was also significantly attenuated in the ELN-rSkM group compared with the control group eight weeks after implantation ($P < 0.05$) (Table 1). The ESV showed a significant decrease in the ELN-rSkM group compared with the control group at both six and eight weeks after implantation (6 weeks $P < 0.05$, 8 weeks $P < 0.01$) (Table 1).

The decline of heart weight/body weight ratio

To evaluate the degree of cardiac hypertrophy, we used the HW/BW ratio as an indicator. HW/BW showed a significant decrease in the ELN-rSkM group compared with the control and WT-rSkM groups ($P < 0.01$ versus control, $P < 0.05$ versus WT-rSkM) (Table 2).

Myoblast sheets secreting elastin exert therapeutic effects on injured myocardium

Victoria blue-HE stained sections demonstrated the occurrence of thinning of the infarcted wall in the control group and the WT-rSkM group, whereas its thickness was maintained in the ELN-rSkM group (Fig. 3; Table 3). A statistical analysis showed that the diameter of the LV chamber was smaller in the ELN-rSkM than in the control or WT-rSkM groups ($P < 0.05$) (Table 3), and that the thickness of the infarcted wall in the ELN-rSkM group was significantly greater than that in the control or WT-rSkM groups ($P < 0.01$) (Table 3). The values of the LV chamber diameter/posterior wall thickness were significantly decreased in the ELN-rSkM group compared with the control group and WT-rSkM group ($P < 0.01$) (Table 3).

Table 2 The heart weight/body weight (HW/BW) ratio at 8 weeks after sheet transplantation

	Body weight (BW) (g)	Heart weight (HW) (mg)	HW/BW
Control	184.97 ± 7.94	763.33 ± 5.53	4.13 ± 0.17
WT-rSkM	184.19 ± 9.01	705.00 ± 5.61	3.83 ± 0.34*
ELN-rSkM	190.88 ± 8.08	677.50 ± 4.77	3.55 ± 0.20**†

* $P < 0.05$, ** $P < 0.01$ versus control. † $P < 0.05$ versus WT-rSkM

Table 3 The thickness of infarcted wall and posterior wall and LV chamber

	Control	WT-rSkM	ELN-rSkM
LV chamber diameter (mm)	4.55 ± 0.52	4.40 ± 0.45	3.81 ± 0.52*†
Infarcted wall thickness (mm)	0.47 ± 0.13	0.49 ± 0.09	0.63 ± 0.13
Posterior wall thickness (mm)	1.82 ± 0.19	1.75 ± 0.27	1.78 ± 0.19
% Anterior wall thickness	26.40 ± 2.96	27.76 ± 2.08	35.88. ± 2.29**‡
LV chamber diameter/ posterior wall thickness	2.50 ± 0.16	2.51 ± 0.18	2.14 ± 0.16**‡

% Anterior wall thickness = infarcted wall thickness/posterior wall thickness ×100 * $P < 0.05$, ** $P < 0.05$, ‡ $P < 0.01$ versus control, † $P < 0.05$, ‡ $P < 0.01$ versus WT-rSkM

There were no significant differences between the control and WT-rSkM groups on these indexes.

In the border area, staining with picrosirius red showed the presence of a significant reduction of fibrosis in the ELN-rSkM group in comparison with the control and WT-rSkM groups ($P < 0.01$) [Figs. 4A(a)–(c), B(a)]. Periodic acid–Schiff staining showed that the diameters of the cardiomyocytes in the ELN-rSkM group were significantly smaller than those in the control or WT-rSkM groups ($P < 0.01$) [Figs. 4A(d)–(f), B(b)].

The vascular density was significantly increased in the WT-rSkM and ELN-rSkM groups compared with the control group ($P < 0.01$), but there were no significant differences between the WT-rSkM and ELN-rSkM groups [Figs. 4A(g)–(i), B(c)]. Fibrosis, cell size, and vascular density were not different in the remote area among three groups.

Increase in the distribution of elastic fibers in epicardial area of implanted area

Victoria blue-HE and Elastica van Gieson stained sections showed that the numbers of elastic fibers were increased in the ELN-rSkM group [Figs. 3c, 5A(c), B(f)]. Recombinant elastin was widely detected throughout the scar area and border zone in the epicardial area of the ELN-rSkM group, and when it was examined at a higher magnification (×200), it was found to form long wavy structures [Fig. 5B(f)]. The layers of formed elastin fiber would have showed the guard ring effect and depressed the dilation of LV chamber. In contrast, it was scarce in the control and WT-rSkM groups [Figs. 3a, b, 5A(a), (b), B(d), (e)].

The alteration of expression of matrix metalloproteinase 1 and 2 by recombinant elastin

The expression of recombinant elastin was only recognized in infarcted areas of the ELN-rSkM group [Fig. 6A, B(a)]. The expression of MMP-1 was increased in border areas of the ELN-rSkM group compared with that in the control and WT-rSkM groups [Fig. 6A, B(b)]. In the control group, expression of MMP-2 was detected in infarcted, border, and remote areas, whereas in the WT-rSkM group, although it was detected in the infarcted area, there was little expression in border and remote areas. In the ELN-rSkM group, expression of MMP-2 was barely detectable in any area [Fig. 6A, B(c)].

Discussion

Elastin is a major insoluble ECM component. The elastic fiber provides elasticity and extensibility to tissue. Elastin fibers consist of a core of tropoelastin together with crosslinked proteins, including microfibril and fibrillin [20–24]. Elastin contains two major repeated peptide sequences: the pentapeptide Gly-Val-Gly-Val-Pro (GVGVP) and the hexapeptide Val-Gly-Val-Ala-Pro-Gly (VGVAPG). GVGVP has elasticity properties, whereas VGVAPG lacks elasticity, but does induce proliferation and migration of fibroblasts and smooth muscle cells [25–28]. It would have been preferable to express the full length of the elastin gene, but rat tropoelastin cDNA (2,595 bp) is a difficult protein to express, and when we attempted to express the full-length protein, we were unable to do so. We therefore chose a 600-bp (1,201–1,800 bps) segment of the rat tropoelastin. The elastic and resilient properties of elastin are located within this fragment [20].

The cell sheets are generated on and removed from special dishes that are coated with a temperature-responsive polymer, poly [*N*-isopropylacrylamide], that changes from hydrophobic to hydrophilic when the temperature is lowered without destroying the cell–cell or cell-ECM adhesions in the cell sheet. Typical cell harvests by means of enzymatic digestion therefore result in the disruption of both adhesive proteins and membrane receptors. The

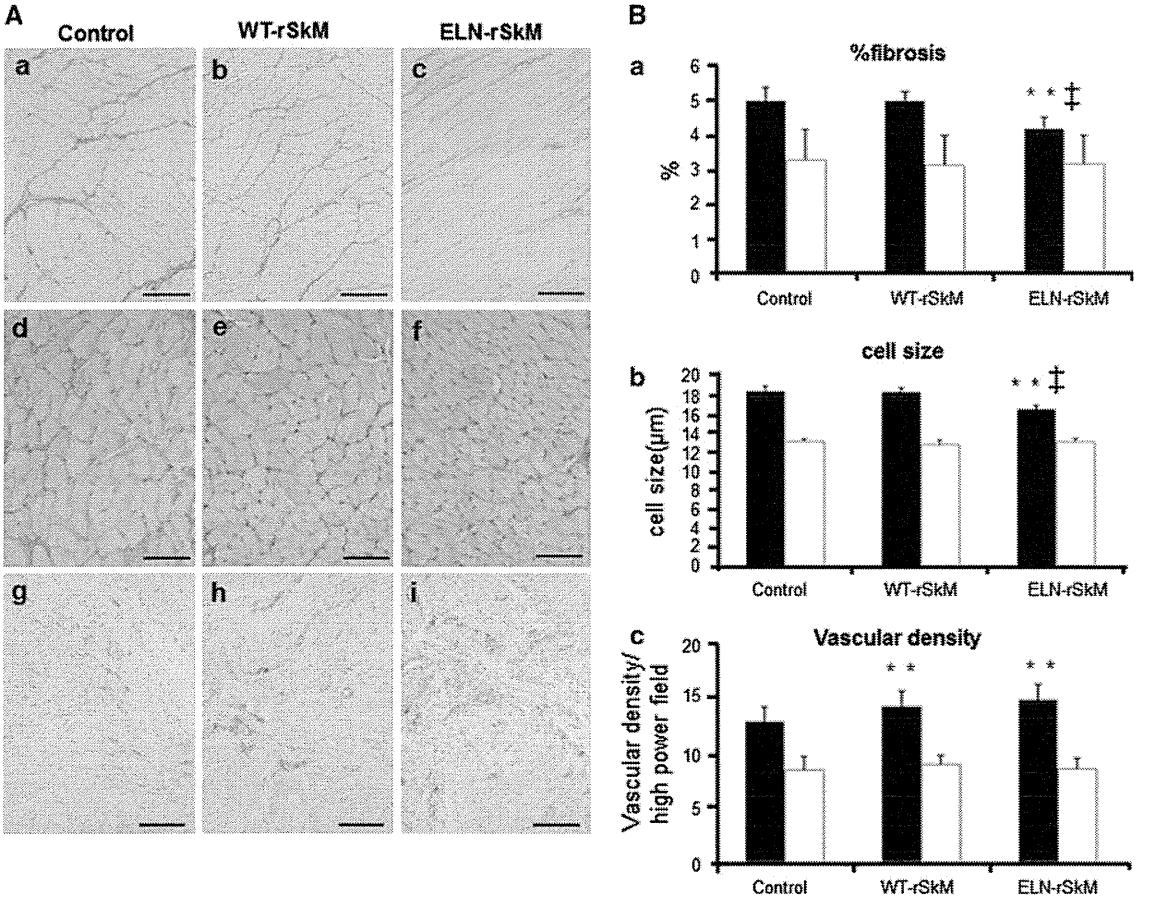

Fig. 4 Histological evaluations of LV remodeling after infarction. **A** Sirius-red stained myocardium of the infarcted border zone *a* control, *b* WT-rSkM *c* ELN-rSkM (×200, *scale bar* 100 μm); periodic acid–Schiff staining of cardiomyocyte of infarcted border zone: *d* control, *e* WT-rSkM, *f* ELN-rSkM (×400, *scale bar* 50 μm); and section of infarcted border zone stained with antibody against Von Willebrand factor: *g* control, *h* WT-rSkM, *i* ELN-rSkM (×200, *scale bar* 100 μm). **B** Quantitative estimation of histological study results: *a* %fibrosis, *b* cell size, *c* vascular density. Histological analysis showed that left ventricular remodeling such as fibrosis and cardiomyocyte hypertrophy were attenuated in the ELN-rSkM group compared with the control and WT-rSkm groups. $^{**}P < 0.01$ versus control. $\dagger P < 0.05$, $\ddagger P < 0.01$ versus WT-rSkM. *Filled bar* border area, *bar* remote area

greatest advantage of this technique is that the sheet is made only of cells, and the cells produce the ECM without requiring an artificial scaffold. The myoblast sheet has a high ability to integrate with area of infarction through the adhesion factors, such as integrin$\alpha 7\beta 1$ and α-dystroglycan, which is expressing on the surface of myoblasts and therefore doesn't fall off after closing the chest.

In this study, we treated hearts, in which MI had been previously induced, by implantation of myoblast sheets that secreted elastin fragments, and we observed continuous improvements in cardiac function and in attenuation of cardiac remodeling. Histological assessment of the ELN-rSkM group showed that elastic fiber was present in both the scarred area and in border zones, whereas this effect was not observed in the control group or the WT-rSkM group. So the accumulation of elastin fibers would be the result of construction of tropoelastin secreted from the transplanted myoblasts.

The dramatic improvements in the left ventricular diastolic and systolic performance in the ELN-rSkM group might be attributable to the formation of elastin fibers in the infarcted region. Accumulation of elastin fibers improved the left ventricular wall movement. The assessments of LVIDd and LVIDs over time showed the continuous depression of dilation of inside diameter in ELN-rSkM group, especially at late points, 6 and 8 weeks after sheet implantation. It is especially noteworthy that the LVIDd in the ELN-rSkM were significantly attenuated 8 weeks after sheet implantation. The myoblast sheets were transplanted into the epicardium and the layers of elastic fiber should have formed epicardial area. Therefore, their guard ring effects might have significantly prevented the outward dilation of the LV chamber in the late stage. And the values of the LV chamber diameter/posterior wall thickness in the ELN-rSkM were significantly smaller than the control and WT-rSkM.

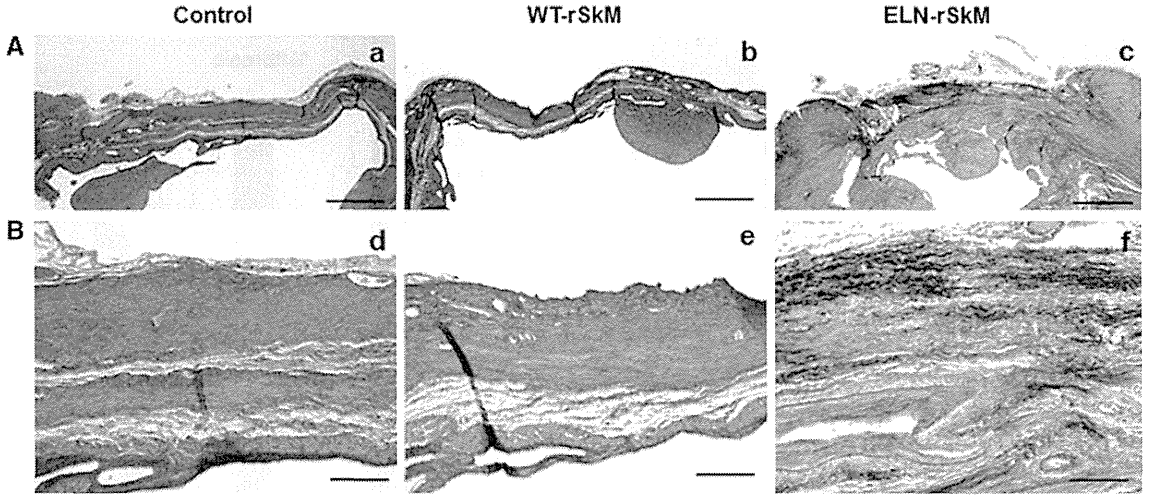

Fig. 5 Elastin distributions in the infarcted area by elastica van Gieson staining and immunohistochemical staining using an antibody against elastin [**A** (*a* control, *b* WT-rSkM, *c* ELN-rSkM, *a–c*, ×20, *scale bar* 500 μm), **B** (*d* control, *e* WT-rSkM, *f* ELN-rSkM, *d–f* ×200, *scale bar* 100 μm)]. Recombinant elastin was widely detected throughout the scar area and border zone in the epicardial area of the ELN-rSkM group

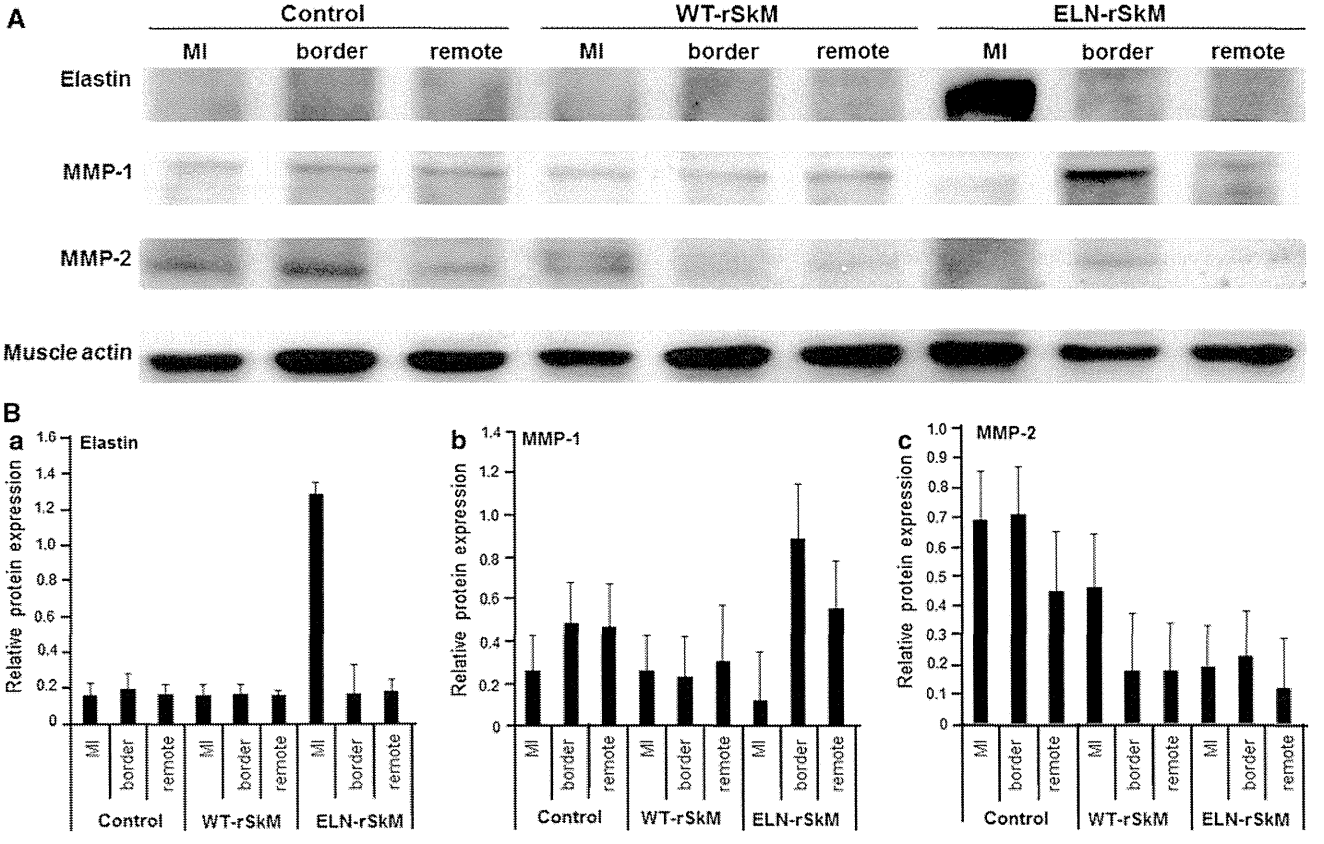

Fig. 6 Expression of elastin, matrix metalloproteinase 1 (MMP-1), and matrix metalloproteinase 2 (MMP-2) examined by western blotting. **A** A representative result of Elastin, MMP-1, and MMP-2 protein expression. **B** Quantitation of western blotting of Elastin, MMP-1, and MMP-2 expression normalized by the corresponding muscle actin expressing levels. *a* Elastin, *b* MMP-1, *c* MMP-2 recombinant elastin was only recognized in infarcted areas of the ELN-rSkM group. The expression of MMP-1 was increased in border areas of the ELN-rSkM group, and the expression of MMP-2 was barely detectable in any area of the ELN-rSkM group compared with that in the control and WT-rSkM groups

Most of the transplanted myoblasts drop out until 4 weeks after sheet transplantation. As a result, cardiac functions such as EF and %FS in the WT-rSkM group was markedly depressed 4 weeks after sheet transplantation. In contrast, because the lifespan of elastin fibers can be measured in years, the elastin fiber that was formed remained after dropout of the transplanted cells and it produced a long-term improvement in cardiac function and attenuation of remodeling. The early therapeutic effects after elastin-secreted myoblast sheets implantation would have been resulted from paracrine growth factors such as VEGF and HGF by myoblasts transplantation, and the late effects have been caused by the guard ring function of the formed elastin fibers.

Additionally, owing to the widespread distribution of recombinant elastin fibers in the border zone, adverse impacts on the uninjured myocardium and their exercise quantity were reduced, and consequently, cardiac remodeling processes, such as fibrosis and cardiomyocyte hypertrophy, were attenuated.

Our study would have been significantly strengthened if we had a longer follow-up period. However, a previous study [15] has shown that the cardiac functions such as EF and %FS have been markedly depressed between 4 and 8 weeks after autologous myoblast sheet transplantation. Therefore, in the present study, we have assessed the cardiac function and histological change such as left ventricular remodeling and deposition of elastic fiber over time up to 8 weeks after sheet implantation.

The ECM exerts an influence on cellular movement and cross-interactions, and elastin is a major structural component of the extracellular matrix. The ratio of collagen to elastin in tissue is involved in a variety of clinical conditions, and both MMP and tissue inhibitor of metalloproteinase (TIMP) modulate this ratio. In curing ischemic cardiac disease, the necrotic myocardium is replaced by collagen fiber, especially type I and type III collagen, and elasticity is lost in the scarred area. There are also a few reports that the elastin-derived hexapeptide VGVAPG stimulates the expression of MMP-1 [29–31]. In the present study, we have shown that an increase in MMP-1 expression occurs in the infarcted area of the ELN-rSkM group at 8 weeks after sheet transplantation. This suggests that the recombinant elastin secreted from the myoblasts increased the expression of MMP-1. Increased expression of MMP-1, which mainly decomposes collagen types I and III, inhibits fibrosis and improves cardiac function [32]. The depression of fibrosis in the ELN-rSkM group could, therefore, be due to an increase in MMP-1 expression by recombinant elastin and upregulation of collagen degradation by MMP-1. Furthermore, in cardiac infarction, the degradation products of collagen, laminin, and fibronectin generated by the activity of MMP-2 stimulate macrophage migration in the infarcted myocardium [33]. The macrophages that migrate into the infarcted tissue are involved in inflammation and in the healing process as a result of their phagocytosis function, promoting cardiac fibrosis and regulating LV remodeling [34]. Furthermore, inhibition of MMP2 activity suppresses LV remodeling after infarction and improves the survival rate after an acute MI. In this study, the levels of expression of MMP-2 in the ELN-rSkM group were decreased in comparison with those in the control group and the WT-rSkM group 8 weeks after implantation. The change in expression levels of MMP-2 by recombinant elastin might therefore repress LV remodeling resulting from ECM degradation of MMP-2. The newly formed elastin fibers might themselves alter the composition of the ECM and affect the expression of MMPs, resulting in inhibition of remodeling of the infarcted heart.

Previous researchers have demonstrated that cardiac disease therapy with myoblast sheets can effect improvements in cardiac function. This study identified elastin, produced in a myoblast sheet transfected with the elastin gene, as a factor that might improve the therapeutic effect of myoblast sheets and thereby improve cardiac function in an ongoing manner. However, further research regarding the number of cells and secretion volume is necessary.

Because autologous myoblast sheet transplantation had shown no adverse effects in either preclinical or clinical tests, it seems feasible to adopt this cell transplantation for gene modification. And, the sheet transplantation can be applied to treatment of serious heart failure, and it gives minimal damage to heart muscle compared with cell injections. And, the myoblast sheet transplantation has no worries of tumorigenesis which occurs during the transplantation of embryo-stem cell or induced pluripotent stem cell. Furthermore, the present study used a lentivirus vector to transfect the elastin gene into primary rat skeletal myoblasts. Attempts to use nonviral transfection techniques did not result in expression of elastin protein. We also examined the muscle cell lines such as smooth muscle cell and skeletal muscle cell, as carriers of the elastin gene, but in the cell line, only the virus vector expressed elastin. For clinical applications, further research will be necessary to identify new methods of gene transfection that do not require the use of a virus vector. The past clinical trials indicate the efficacy of myoblast sheet transplantation, and the gene modification of the implanted myoblast is also expected to improve the long-term results of the treatment in the clinical application.

In summary, we have shown that the implantation of elastin-secreting myoblast sheets continuously improved cardiac function, and inhibited cardiac remodeling and dilation of the LV chamber. The functional myoblast sheets to which the elastin gene was transfected improved the long-term treatment result. The recombinant elastin fibers

were formed in the epicardial area so that dilation of the left ventricular chamber after MI was prevented. The early therapeutic effects after elastin-secreted myoblast sheets implantation would have been resulted from paracrine growth factor by transplanted myoblasts, and the late effects have been caused by the guard ring function of the formed elastin fibers. The therapeutic effect of myoblast sheets can be further enhanced by gene therapy using elastin.

Acknowledgments We thank Ibu Matsuzaki and Aya Nakayama for excellent technical assistance.

References

1. Akhyari P, Fedak PWV, Weisel RD, Lee JYJ, Verma S, Mickle DAG, Li RK (2002) Mechanical stretch regimen enhances the formation of bioengineered autologous cardiac muscle grafts. Circulation 106:137–142
2. Hamano K, Nishida M, Hirata K, Mikamo A, Li TS, Harada M, Miura T, Matsuzaki M, Esato K (2001) Local implantation of autologous bone marrow cells for therapeutic angiogenesis in patients with ischemic heart disease. Circ J 65:845–847
3. Tang XL, Rokosh DG, Guo Y, Bolli R (2010) Cardiac progenitor cells and bone marrow-derived very small embryonic-like stem cells for cardiac repair after myocardial infarction. Circ J 74:390–404
4. Chazaud B, Hittinger L, Sonnet C, Champagne S, Le Corvoisier P, Benhaiem-Sigaux N, Unterseeh T, Su J, Merlet P, Rahmouni A, Garot J, Gherardi R, Teiger E (2003) Endoventricular porcine autologous myoblast transplantation can be successfully achieved with minor mechanical cell damage. Cardiovasc Res 58:444–450
5. Pagani FD, DerSimonian H, Zawadzel A, Wetzel K, Edge AS, Jacoby DB (2003) Autologous skeletal myoblast transplanted to ischemia-damaged myocardium in human. J Am Coll Cardiol 41:879–888
6. Premaratne GU, Tambara K, Fujita M, Lin X, Kanemitsu N, Tomita S, Sakaguchi G, Nakajima H, Ikeda T, Komeda M (2006) Repeated implantation is a more effective cell delivery method in skeletal myoblast transplantation for rat myocardial infarction. Circ J 70:1184–1189
7. Memon IA, Sawa Y, Miyagawa S, Taketani S, Matsuda H (2005) Combined autologous cellular cardiomyoplasty with skeletal myoblasts and bone marrow cells in canine hearts for ischemic cardiomyopathy. J Thorac Cardiovasc Surg 130:646–653
8. Memon IA, Sawa Y, Fukushima N, Matsumiya G, Miyagawa S, Taketani S, Sakakida SK, Kondoh H, Aleshin AN, Shimizu T, Okano T, Matsuda H (2005) Repair of impaired myocardium by means of implantation of engineered autologous myoblast sheets. J Thorac Cardiovasc Surg 130:1333–1341
9. Suzuki K, Murtuza B, Fukushima S, Smolenski RT, Varela-Carver A, Coppen SR (2004) Targeted cell delivery into infarcted rat hearts by retrograde intracoronary infusion: distribution, dynamics, and influence on cardiac function. Circulation 110:225–230
10. Fernandes S, Amirault JC, Lande G, Nguyen JM, Forest V, Bignolais O, Lamirault G, Heudes D, Orsonneau JL, Heymann MF, Charpentier F, Lemarchand P (2006) Autologous myoblast transplantation after myocardial infarction increases the inducibility of ventricular arrhythmias. Cardiovasc Res 69:348–358
11. Okano T, Yamada N, Okuhara M, Sakai H, Sakurai Y (1995) Mechanism of cell detachment from temperature-modulated, hydrophilic-hydrophobic polymer surfaces. Biomaterials 16: 297–303
12. Miyagawa S, Sawa Y, Kitabayashi-Sakakida S, Taketani S, Memon IA, Kondoh H (2005) Tissue cardiomyoplasty using bioengineered contractile cardiomyocytes sheets to repair damaged myocardium: their integration with recipient myocardium. Transplantation 80:1586–1595
13. Kondoh H, Sawa Y, Miyagawa S, Sakakida-Kitagawa S, Memon IA, Kawaguchi N, Matsuura N, Shimizu T, Okano T, Matsuda H (2006) Longer preservation of cardiac performance by sheet-shaped myoblast implantation in dilated cardiomyopathic hamsters. Cardiovasc Res 69:466–475
14. Hata H, Matsumiya G, Miyagawa S, Kondoh H, Kawaguchi N, Matsuura N, Shimizu T, Okano T, Matsuda H, Sawa Y (2006) Grafted skeletal myoblast sheets attenuate myocardial remodeling in pacing-induced canine heart failure model. J Thorac Cardiovasc Surg 132:918–924
15. Sekiya N, Matsumiya G, Miyagawa S, Saito A, Shimizu T, Okano T, Kawaguchi N, Matsuura N, Sawa Y (2009) Layered implantation of myoblast sheets attenuates adverse cardiac remodeling of the infracted heart. J Thorac Cardiovasc Sur 138:985–993
16. Gupta KB, Ratcliffe MB, Fallert MA, Edmunds LH Jr, Bogen DK (1994) Changes in passive mechanical stiffness of myocardial tissue with aneurysm formation. Circulation 89:2315–2326
17. Pfeffer MA, Braunwald E (1990) Ventricular remodeling after myocardial infarction. Experimental observations and clinical implications. Circulation 81:1161–1172
18. Mizuno T, Yau TM, Weisel RD, Kiani CG, Li RK (2005) Elastin stabilizes an infarct and preserves ventricular function. Circulation 112:81–88
19. Mizuno T, Mickle DA, Kiani CG, Li RK (2005) Overexpression of elastin fragments in infracted myocardium attenuates scar expansion and heart dysfunction. Am J Physiol Heart Circ Physiol 288:2819–2827
20. Keeley FW, Bellingham CM, Woodhouse KA (2002) Elastin as a self-organizing biomaterial: use of recombinantly expressed human elastin polypeptides as a model for investigations of structure and self-assembly of elastin. Philos Trans R Soc Lond B Biol Sci 357:185–189
21. Li DY, Brooke B, Davis EC, Mecham RP, Sorensen LK, Boak BB, Eichwald E, Keating MT (1998) Elastin is an essential determinant of arterial morphogenesis. Nature 393:276–280
22. Nakamura T, Lozano PR, Ikeda Y, Iwanaga Y, Hinek A, Minamisawa S, Cheng CF, Kobuke K, Dalton N, Takada Y, Tashiro K, Ross J Jr, Honjo T, Chien KR (2002) Fibulin-5/DANCE is essential for elastogenesis in vivo. Nature 415:171–175
23. Pereiral L, Lee SY, Gayraud B, Andrikopouls K, Shapiro SD, Bunton T, Biery NJ, Dietz HC, Sakai LY, Ramirez F (1999) Pathogenetic sequence for aneurysm revealed in mice underexpressing fibrillin-1. Proc Natl Acad Sci USA 96:3819–3823
24. Yanagisawa H, Davis EC, Starcher BC, Ouchi T, Yanagisawa M, Richardson JA, Olson EN (2002) Fibulin-5 is an elastin-binding protein essential for elastin fiber development in vivo. Nature 415:168–171
25. Kamoun A, Landeau JM, Godeau G, Wallach J, Duchesnay A, Pellat B, Hornebeck W (1995) Growth stimulation of human skin fibroblasts by elastin-derived peptides. Cell Adhes Commun 3:273–281
26. Wachi H, Seyama Y, Yamashita S, Suganami H, Uemura Y, Okamoto K, Yamada H, Tajima S (1995) Stimulation of cell proliferation and autoregulation of elastin expression by elastin peptide VPGVG in cultured chick vascular smooth muscle cells. FEBS Lett 368:215–219
27. Tajima S, Wachi H, Seyama Y (1996) Tropoelastin-derived degradation products down-regulate elastin expression in vascular smooth muscle cell in culture. Connect Tissue 28:231–235

28. Mecham RP, Hinek A, Entwistle R, Wrenn DS, Griffin GL, Senior RM (1989) Elastin binds to a multifunctional 67 kilodalton peripheral membrane protein. Biochemistry 28:3716–3722
29. Tyagi SC, Kumar SG, Alla SR, Reddy HK, Voelker DJ, Janicki JS (1996) Extracellular matrix regulation of metalloproteinase and antiproteinase in human heart fibroblast cells. J Cell Physiol 167:137–147
30. Brassart B, Fuchs P, Huet E, Alix AJ, Wallach J, Tamburro AM, Delacoux F, Haye B, Emonard H, Hornebeck W, Debelle L (2001) Conformational dependence of collagenase (matrix metalloproteinase-1) up-regulation by elastin peptides in cultured fibroblasts. J Biol Chem 276:5222–5227
31. Booms P, Ney A, Barthel F, Moroy G, Counsell D, Gille C, Guo G, Pregla R, Mundlos S, Alix AJ, Robinson PN (2006) A fibrillin-1-fragment containing the elastin-binding-protein GxxPG consensus sequence upregulates matrix metalloproteinase-1: biochemical and computational analysis. J Mol Cell Cardiol 40: 234–246
32. Lin X, Jo H, Ishii TM, Fujita M, Fu M, Tambara K, Yamamoto M, Tabata Y, Komeda M, Matsuoka S (2009) Controlled release of matrix metalloproteinase-1 plasmid DNA prevents left ventricular remodeling in chronic myocardial infarction of rats. Circulation 73:2315–2321
33. Matsumura S, Iwanaga S, Mochizuki S, Okamoto H, Ogawa S, Okada Y (2005) Targeted deletion or pharmacological inhibition of MMP-2 prevents cardiac rupture after myocardial infarction in mice. J Clin Invest 115:599–609
34. Noji Y, Shimizu M, Ino H, Higashikata T, Yamaguchi M, Nohara A, Horita T, Shimizu K, Ito Y, Matsuda T, Namura M, Mabuchi H (2004) Increased circulating matrix metalloproteinase-2 in patients with hypertrophic cardiomyopathy with systolic dysfunction. Circ J 68:355–360

Moriyama et al. BMC Cell Biology 2012, 13:21
http://www.biomedcentral.com/1471-2121/13/21

BMC Cell Biology

RESEARCH ARTICLE Open Access

Human adipose tissue-derived multilineage progenitor cells exposed to oxidative stress induce neurite outgrowth in PC12 cells through p38 MAPK signaling

Mariko Moriyama[1,2†], Hiroyuki Moriyama[1*†], Ayaka Ueda[1], Yusuke Nishibata[1], Hanayuki Okura[2], Akihiro Ichinose[3], Akifumi Matsuyama[2] and Takao Hayakawa[1]

Abstract

Background: Adipose tissues contain populations of pluripotent mesenchymal stem cells that also secrete various cytokines and growth factors to support repair of damaged tissues. In this study, we examined the role of oxidative stress on human adipose-derived multilineage progenitor cells (hADMPCs) in neurite outgrowth in cells of the rat pheochromocytoma cell line (PC12).

Results: We found that glutathione depletion in hADMPCs, caused by treatment with buthionine sulfoximine (BSO), resulted in the promotion of neurite outgrowth in PC12 cells through upregulation of bone morphogenetic protein 2 (BMP2) and fibroblast growth factor 2 (FGF2) transcription in, and secretion from, hADMPCs. Addition of *N*-acetylcysteine, a precursor of the intracellular antioxidant glutathione, suppressed the BSO-mediated upregulation of BMP2 and FGF2. Moreover, BSO treatment caused phosphorylation of p38 MAPK in hADMPCs. Inhibition of p38 MAPK was sufficient to suppress BMP2 and FGF2 expression, while this expression was significantly upregulated by overexpression of a constitutively active form of MKK6, which is an upstream molecule from p38 MAPK.

Conclusions: Our results clearly suggest that glutathione depletion, followed by accumulation of reactive oxygen species, stimulates the activation of p38 MAPK and subsequent expression of BMP2 and FGF2 in hADMPCs. Thus, transplantation of hADMPCs into neurodegenerative lesions such as stroke and Parkinson's disease, in which the transplanted hADMPCs are exposed to oxidative stress, can be the basis for simple and safe therapies.

Keywords: Human adipose-derived multilineage progenitor cells, Adult stem cells, Reactive oxygen species, p38 MAPK, Neurite outgrowth, BMP2, FGF2, Neurodegenerative disorders

Background

Mesenchymal stem cells (MSCs) are pluripotent stem cells that can differentiate into various types of cells [1-6]. These cells have been isolated from bone marrow [1], umbilical cord blood [2], and adipose tissue [3-6] and can be easily obtained and expanded *ex vivo* under appropriate culture conditions. Thus, MSCs are an attractive material for cell therapy and tissue engineering. Human adipose tissue-derived mesenchymal stem cells, also referred to as human adipose tissue-derived multilineage progenitor cells (hADMPCs), are especially advantageous because they can be easily and safely obtained from lipoaspirates, and the ethical issues surrounding other sources of stem cells can be avoided [4-6]. Moreover, hADMPCs have more pluripotent properties for regenerative medical applications than other stem cells, since these cells have been reported to have the ability to migrate to the injured area and differentiate into hepatocytes [4], cardiomyoblasts [5], pancreatic cells [7], and neuronal cells [8-10]. In addition, it is known that hADMPCs secrete a wide variety of cytokines and

* Correspondence: moriyama@phar.kindai.ac.jp
†Equal contributors
[1]Pharmaceutical Research and Technology Institute, Kinki University, 3-4-1 Kowakae, Higashi-Osaka, Osaka 577-8502, Japan
Full list of author information is available at the end of the article

growth factors necessary for tissue regeneration including nerve growth factor (NGF), brain-derived neurotrophic factor (BDNF), fibroblast growth factors (FGFs), vascular endothelial growth factor (VEGF) and hepatocyte growth factor (HGF) [11-14].

Recently, several groups have reported that hADMPCs facilitate neurological recovery in experimental models of stroke [9,10,15] and Parkinson's disease [16]. Despite the superiority of hADMPCs over other stem cells, the potential use of hADMPCs for the treatment of these neurodegenerative disorders has not been fully investigated. It has been reported that administration of hADMPCs in animal models of acute ischemic stroke markedly decreased brain infarct size, improved neurological function by enhancing angiogenesis and neurogenesis, and showed anti-inflammatory and anti-apoptotic effects [9,10]. These effects were due in part to increased secretion levels of VEGF, HGF and bFGF under hypoxic conditions [13], indicating the role of hADMPCs in reducing the severity of hypoxia-ischemic lesions.

In addition to hypoxic stress, ischemic lesions are generally subject to inflammation, which leads to the generation of reactive oxygen species (ROS) [17,18]. ROS are

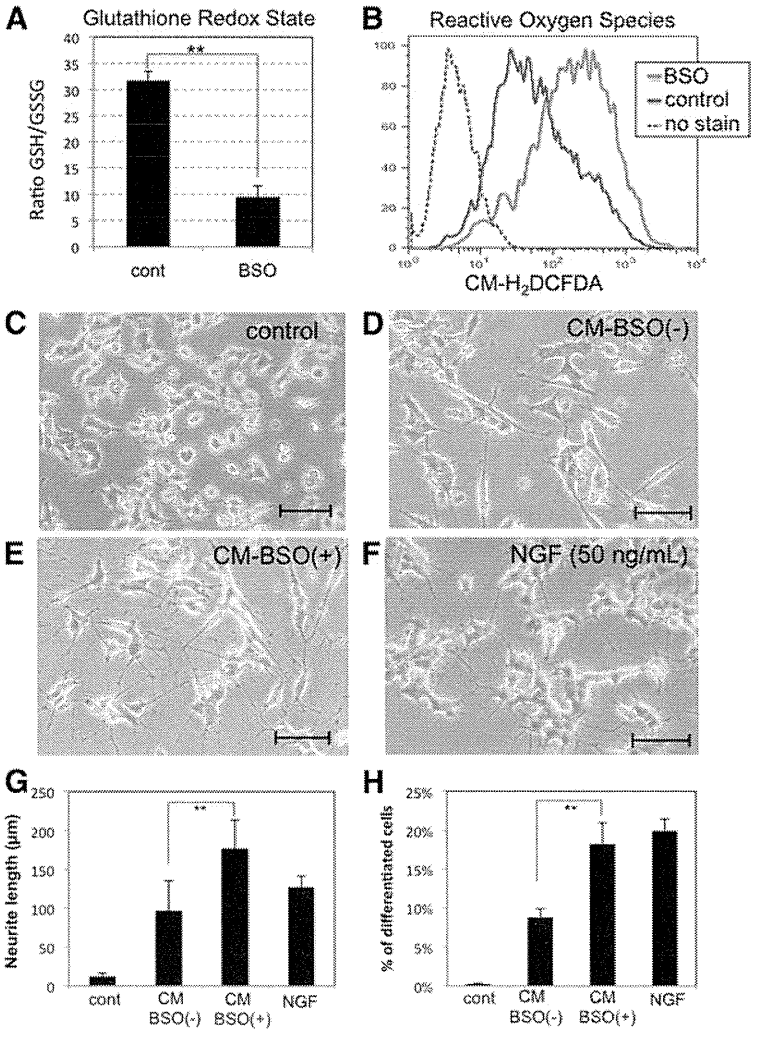

Figure 1 Conditioned medium from hADMPCs exposed to oxidative stress induces neurite outgrowth in PC12 cells. (A, B) Decrease of the reduced/oxidized glutathione ratios and increase in the intracellular ROS levels in hADMPCs treated with BSO. hADMPCs were treated with 1 mM BSO for 16 h, and cellular GSH/GSSG levels (**A**) or ROS (H_2O_2) levels (**B**) were analyzed. **(C-G)** Induction of neurite outgrowth in PC12 cells by conditioned medium from BSO-treated hADMPCs. PC12 cells were induced to differentiation by changing medium to differentiation medium alone (**C**), CM-BSO (−) (**D**), CM-BSO (+) (**E**), or differentiation medium with NGF (50 ng/mL) (**F**) for 2 days. Scale bars, 200 μm. (**G**) One hundred individual neurites were measured in each sample using Dynamic Cell Count Analyzer BZ-H1C (Keyence, Osaka, Japan) and average neurite length was calculated. **, $P < 0.01$ (Student's t test). **(H)** Percentage of neurite-bearing PC12 cells. A cell was scored positive for bearing neurites if it has a thin neurite extension that is double the length of the cell body diameter. A total of 500–600 cells in each sample were counted. **, $P < 0.01$ (Student's t test).

generated as a natural byproduct of normal aerobic metabolism, and mitochondrial respiration, together with oxidative enzymes such as plasma membrane oxidase, is considered to be the major intracellular source of ROS production [19]. Although appropriate levels of ROS play an important role in several physiological processes, oxidative damage initiated by excessive ROS causes many pathological conditions including inflammation, atherosclerosis, aging, and cancer. Neuronal cells are especially vulnerable to oxidative stress, and numerous studies have examined the crucial roles of oxidative stress in neurodegenerative disorders such as stroke [17,18], Alzheimer's disease [20,21], and Parkinson's disease [22,23]. In these diseases, microglia, the macrophages of the central nervous system (CNS), are activated in response to a local inflammation [24] and generate large amounts of reactive oxygen and nitrogen species, thereby exposing nearby neurons to stress [18,25]. Thus, the influence of oxidative stress generated by neurodegenerative lesion on hADMPCs needs to be further studied.

In this study, we examined the role of oxidative stress on hADMPCs in neurite outgrowth in cells of the rat pheochromocytoma cell line (PC12). Upon treatment with buthionine sulfoximine (BSO), an inhibitor of the rate-limiting enzyme in the synthesis of glutathione, hADMPCs accumulated ROS, which resulted in the upregulation of expression levels of the neurotrophic factors BMP2 and FGF2. Our present data thus provide new insights into understanding the mechanism of how hADMPCs exposed to oxidative stress contribute to neurogenesis, and this may explain the effects of stem cell transplantation therapy with hADMPCs in treating ischemic stroke.

Results

hADMPCs exposed to oxidative stress stimulate neurite outgrowth in PC12 cells

hADMPCs were treated with 1 mM BSO for 24 h; a group of hADMPCs that were not given any treatment was used as the control group. As shown in Figure 1A and B, BSO treatment resulted in significant reduction of intracellular reduced glutathione levels, followed by accumulation of intracellular reactive oxygen species (ROS) in hADMPCs. To investigate whether accumulation of ROS affects secretion of cytokines from hADMPCs, conditioned medium from BSO-treated (CM-BSO (+)) or BSO-untreated (CM-BSO (–)) hADMPCs was added to PC12 cells. As expected, addition of NGF significantly induced neurite outgrowth in the PC12 cells (Figure 1F, G, H). hADMPCs, like other mesenchymal stem cells derived from bone marrow or adipose tissue, may secrete many cytokines including NGF, BDNF and FGF2, and this may account for the slight induction of neurite outgrowth seen in the CM-BSO (–) treated cells (Figure 1D, G, H). In contrast, the number and length of neurite outgrowth of PC12 cells in CM-BSO (+) (Figure 1E) was markedly enhanced compared with those in CM-BSO (–) (Figure 1D, E, G, H).

Conditioned medium from BSO-treated hADMPCs activates Erk1/2 MAPK and Smad signaling in PC12 cells

To investigate which intracellular signaling pathways were involved in the neurite outgrowth of PC12 cells in CM-BSO (+), we used western blotting to determine the phosphorylation levels of Erk1/2 MAPK, p38 MAPK, Smad1/5/8 and Akt in PC12 cells in various culture conditions. NGF significantly activated Erk1/2 MAPK and Akt signaling pathway (Figure 2). In contrast, Erk1/2 MAPK was not activated in PC12 cells exposed to CM-BSO (–), while an increase in phosphorylated Smad1/5/8 was observed. Interestingly, CM-BSO (+) treatment led to both a significant increase in Smad1/5/8 phosphorylation levels as well as activation of the Erk1/2 MAPK

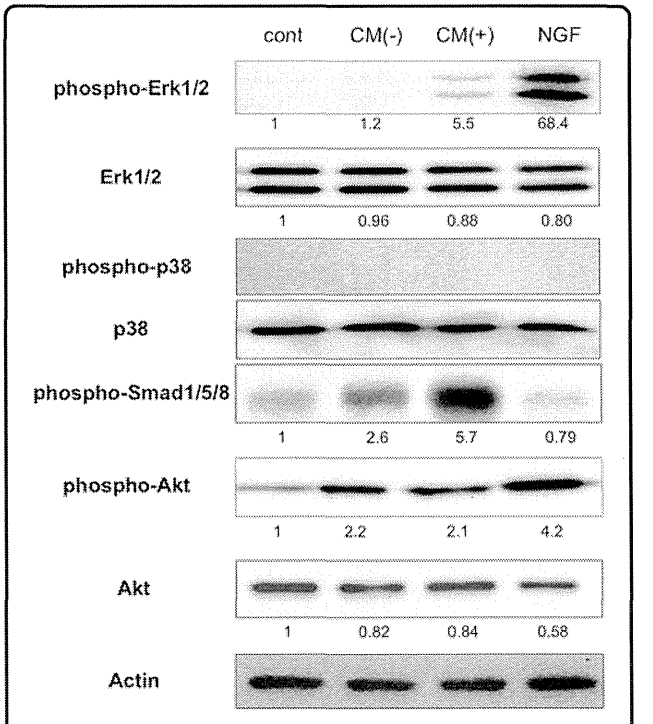

Figure 2 Erk1/2 MAPK and Smad1/5/8 are activated in PC12 cells cultured in conditioned medium from BSO-treated hADMPCs. Western blot analysis of PC12 cells cultured in differentiation medium alone (cont), CM-BSO (–), CM-BSO (+), or differentiation medium with NGF (50 ng/mL) for 1 h. Proteins extracted from each cell culture were resolved by SDS-PAGE, transferred to a membrane, and probed with anti-phosphorylated Erk1/2 (phospho Erk1/2), anti-Erk1/2, anti-phosphorylated p38 (phospho p38), anti-p38, anti-phosphorylated Smad1/5/8 (phospho Smad1/5/8), anti-phosphorylated Akt (phospho Ark) and anti-Akt. Actin was analyzed as an internal control. Numbers below blots indicate relative band intensities as determined by the ImageJ software.